








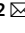




# Memory-enhancing properties of sleep depend on the oscillatory amplitude of norepinephrine

Celia Kjaerby<sup>1,7</sup>  , Mie Andersen<sup>1,7</sup> , Natalie Hauglund<sup>1</sup> , Verena Untiet<sup>1</sup> , Camilla Dall<sup>1</sup>, Björn Sigurdsson<sup>1</sup> , Fengfei Ding<sup>2,3</sup>, Jiesi Feng<sup>4</sup>, Yulong Li<sup>4,5,6</sup> , Pia Weikop<sup>1</sup>, Hajime Hirase<sup>1</sup>  and Maiken Nedergaard<sup>1,2</sup>  

**Sleep has a complex micro-architecture, encompassing micro-arousals, sleep spindles and transitions between sleep stages. Fragmented sleep impairs memory consolidation, whereas spindle-rich and delta-rich non-rapid eye movement (NREM) sleep and rapid eye movement (REM) sleep promote it. However, the relationship between micro-arousals and memory-promoting aspects of sleep remains unclear. In this study, we used fiber photometry in mice to examine how release of the arousal mediator norepinephrine (NE) shapes sleep micro-architecture. Here we show that micro-arousals are generated in a periodic pattern during NREM sleep, riding on the peak of locus-coeruleus-generated infraslow oscillations of extracellular NE, whereas descending phases of NE oscillations drive spindles. The amplitude of NE oscillations is crucial for shaping sleep micro-architecture related to memory performance: prolonged descent of NE promotes spindle-enriched intermediate state and REM sleep but also associates with awakenings, whereas shorter NE descents uphold NREM sleep and micro-arousals. Thus, the NE oscillatory amplitude may be a target for improving sleep in sleep disorders.**

A ample research has documented a rich microstructural organization of sleep, based on EEG activity patterns. For instance, NREM sleep encompasses both delta-dominated and spindle-rich epochs<sup>1</sup>, the latter characterized by frequent appearances of sigma oscillations (8–15 Hz) bursts. Spindles are thought to play a role in post-sleep performance through the promotion of memory consolidation processes<sup>1,2</sup> and often increase in appearance before transition to REM sleep—a phenomenon known as intermediate state (IS) sleep. Uninterrupted sleep is considered important for restorative processes and next-day performance; still, transient arousals, known as micro-arousals, are increasingly recognized as an intrinsic component of normal sleep micro-architecture<sup>3,4</sup>. External induction of micro-arousals in healthy young individuals worsens performance<sup>5</sup>, and conditions associated with frequent micro-arousals, such as aging and dementia, display spindle reduction and cognitive decline<sup>6–8</sup>. Nonetheless, how micro-arousals and memory-enhancing processes, such as spindles, are interconnected and controlled is unknown.

Sleep–wake transitions are orchestrated by several wake-promoting and sleep-promoting regulatory systems<sup>9</sup>, among which the neuromodulator NE released from the locus coeruleus (LC) is intimately linked to wakefulness and attention<sup>10–15</sup>. LC activity is strongly reduced during sleep<sup>11,13,14,16,17</sup>, and extracellular NE is highest during wake, lower during NREM sleep and lowest during REM sleep<sup>18,19</sup>. However, the LC-NE system has not been shown to shape sleep micro-architecture<sup>13,14,16,17,20</sup>, although differential LC-NE activity during NREM sleep has been implicated in the termination of sleep spindles<sup>11,21–25</sup>. Spindle activity has been demonstrated to slowly oscillate during NREM sleep<sup>23</sup>. In this study, we tested the

hypothesis that oscillatory LC-NE-mediated activity during sleep is responsible for the generation of both micro-arousals and the memory-improving spindle activity. A corollary of this hypothesis is that the oscillatory amplitude of NE, rather than the absolute level, shapes the micro-architecture of sleep.

Until now, technical and temporal constraints of electrochemical and microdialysis-based NE measurements have limited insight into the dynamics between extracellular NE levels and the micro-architecture of sleep. In this study, we took advantage of a fluorescent NE biosensor<sup>26</sup> and population-based LC Ca<sup>2+</sup> imaging to make high temporal resolution measurements of the LC-NE system and correlate it with the distinct phases of sleep. Our observations reveal that periodic LC activity during NREM sleep drives infraslow (~30 s) extracellular NE oscillations that are responsible for a cyclic pattern of intrinsic micro-arousals, with only a small fraction of the oscillations resulting in awakening. Intriguingly, we demonstrate that the amplitude of NE oscillations tunes the microstructural organization of sleep related to memory performance: the descending phase of NE oscillations drives spindle activity, and increased descent amplitude promotes spindle-rich IS and REM sleep transition. The NE descent amplitude also determines the size of the successive LC activation and the resulting behavioral outcome. Specifically, long NE descents result in large LC activation and full awakenings, whereas shorter NE descents lead to more subtle LC activation, causing micro-arousals rather than awakenings. Induction of NE descent by LC optogenetic suppression enhances memory performance, whereas pharmacological and optogenetic reduction of NE oscillation amplitude worsens memory performance. In conclusion, we demonstrate a novel and critical role of

<sup>1</sup>Division of Glial Disease and Therapeutics, Center for Translational Neuromedicine, University of Copenhagen, Copenhagen, Denmark. <sup>2</sup>Division of Glial Disease and Therapeutics, Center for Translational Neuromedicine, Department of Neurosurgery, University of Rochester Medical Center, Rochester, NY, USA. <sup>3</sup>Department of Pharmacology, Shanghai Medical College, Fudan University, Shanghai, China. <sup>4</sup>State Key Laboratory of Membrane Biology, Peking University School of Life Sciences, Beijing, China. <sup>5</sup>PKU-IDG/McGovern Institute for Brain Research, Beijing, China. <sup>6</sup>Peking-Tsinghua Center for Life Sciences, Academy for Advanced Interdisciplinary Studies, Peking University, Beijing, China. <sup>7</sup>These authors contributed equally: Celia Kjaerby, Mie Andersen. ✉e-mail: [celia.kjaerby@sund.ku.dk](mailto:celia.kjaerby@sund.ku.dk); [nedergaard@sund.ku.dk](mailto:nedergaard@sund.ku.dk)

NE oscillations in shaping sleep micro-architecture and identify manipulations that directly enhance memory-promoting segments of sleep.

## Results

**Increased NE descent amplitude primes awakenings over micro-arousals.** To dissect the role of LC-NE in shaping the micro-architecture of sleep, we combined fiber photometry with EEG and EMG measurements and correlated real-time LC activity with NE level in the medial prefrontal cortex (mPFC) during sleep (Fig. 1a,b). LC activity was recorded by imaging of GCaMP6f, which was delivered by adeno-associated virus (AAV) injection in TH-Cre transgenic mice, whereas an improved version of the NE biosensor GRAB<sub>NE2m</sub><sup>26</sup> was expressed in mPFC neurons to image NE dynamics (Fig. 1a and Supplementary Fig. 1). Before collection of data, the sensitivity of prefrontal GRAB<sub>NE2m</sub> toward NE and not dopamine in the mPFC was assessed (Supplementary Fig. 2).

Continuous recordings covering multiple sleep-wake episodes revealed that a pronounced infraslow oscillatory pattern<sup>27</sup> dominated the mPFC NE dynamics during NREM sleep (Fig. 1b,c), which was not observed with an NE-insensitive version of the GRAB sensor (Supplementary Fig. 3)<sup>26</sup>. The NE ascends correlated with bursts of LC activity, and NE slowly descended between episodes of LC activity with a periodicity of ~30 seconds (frequency of  $0.034 \pm 0.004$  Hz; Fig. 1c,d and Extended Data Fig. 1e). The NE oscillations had a mean amplitude of  $3.1 \pm 0.5\%$  during NREM sleep and  $5.2 \pm 1.1\%$  during REM sleep, where a continuous NE descent was observed (Fig. 1d). We speculated that this non-stationary nature of NE levels provides a novel way of dissecting the complex nature of sleep micro-architecture. The oscillatory NE ascents during NREM sleep were subdivided into those resulting in wakefulness (>15 seconds, wake<sup>EEG/EMG</sup>) or micro-arousals (<15 seconds, MA<sup>EEG/EMG</sup>) (Fig. 1e). Interestingly, NE ascents that were not accompanied by EMG changes still produced reductions in EEG amplitudes across theta and sigma frequencies (Extended Data Fig. 1), which are established EEG-based criteria for micro-arousals<sup>28</sup>. We, thus, termed these transitions micro-arousals<sup>NE</sup> (MAs<sup>NE</sup>) (Fig. 1e). Only 7.9% of all NE ascents during NREM sleep resulted in awakenings, whereas 29.2% and 63% were associated with MA<sup>EEG/EMG</sup> and MA<sup>NE</sup>, respectively (Fig. 1f). These observations indicate that intrinsic LC-driven NE fluctuations drive a cyclic pattern of micro-arousals during sleep, and only a minority result in awakenings.

As expected, onset of LC activity bouts preceded NE ascents, and the amplitude of LC responses were highest during wake<sup>EEG/EMG</sup> and similar between MA<sup>NE</sup> and MA<sup>EEG/EMG</sup> transitions (Fig. 1g-i). Surprisingly, even though the slope of the NE descent

before the LC activity bouts were similar across all state transitions (Fig. 1j,k), the duration of the descent was longer before awakening, resulting in lower NE trough levels before awakening compared to micro-arousals (Fig. 1l,m). The subsequent NE ascent amplitude and rise time were higher for awakenings compared to micro-arousals (Fig. 1n and Extended Data Fig. 1c,d), which associated with the higher wake-related LC response amplitude (Fig. 1h,i).

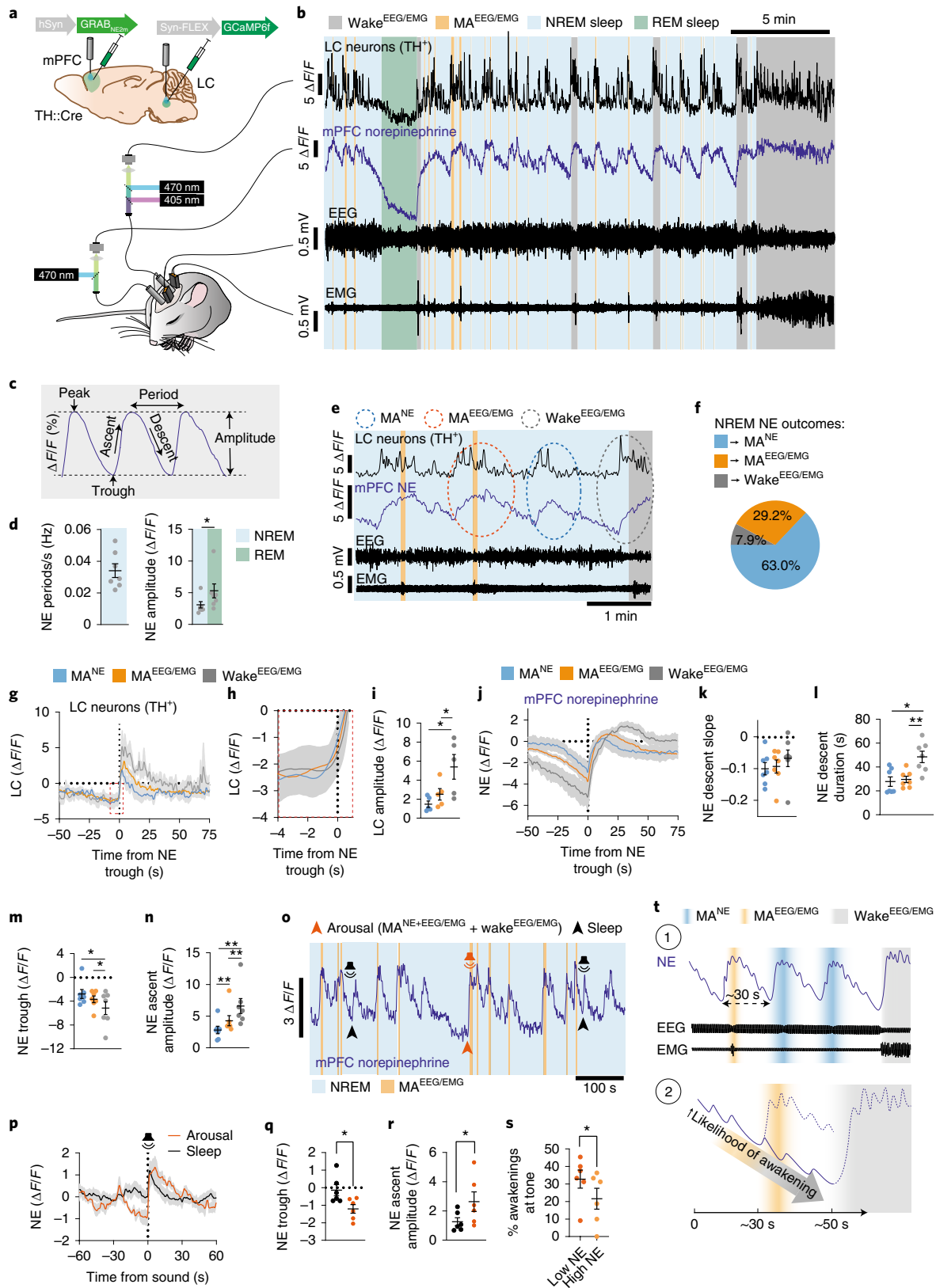
Based on the observation of lower NE trough levels before awakenings, we wondered if NE level could predict the sensitivity toward arousal input. To test this hypothesis, mice were exposed to auditory stimulations (0.5 seconds) during sleep (Fig. 1o). To include all arousals independently of EMG, we used reductions in EEG sigma power to divide tone outcome into arousal and sustained sleep (Fig. 1o and Extended Data Fig. 2), previously validated to be a consistent EEG component of micro-arousals (Extended Data Fig. 1). This analysis showed that the NE trough level was lower before tones that resulted in arousal compared to those that did not (Fig. 1q). Although NE signals during maintained sleep also responded to the tone and reached similar peak values, the amplitude of the NE ascent was lower (Fig. 1r). This observation points to the novel concept that NE amplitude, rather than the peak level of NE, determines arousal. To investigate whether the likelihood of tone-induced awakenings could be predicted based solely on the amplitude of the NE descent, we divided trials into high or low NE trough values (above or below mean) before the tone. This analysis showed that low NE trough levels were predictive of sound-evoked awakenings during NREM sleep (Fig. 1s). In conclusion, we demonstrate that (1) infraslow NE oscillations during NREM sleep coincide with regular micro-arousals, suggesting a causal relationship, and (2) that larger amplitudes of NE descent increase the likelihood of awakening (Fig. 1t).

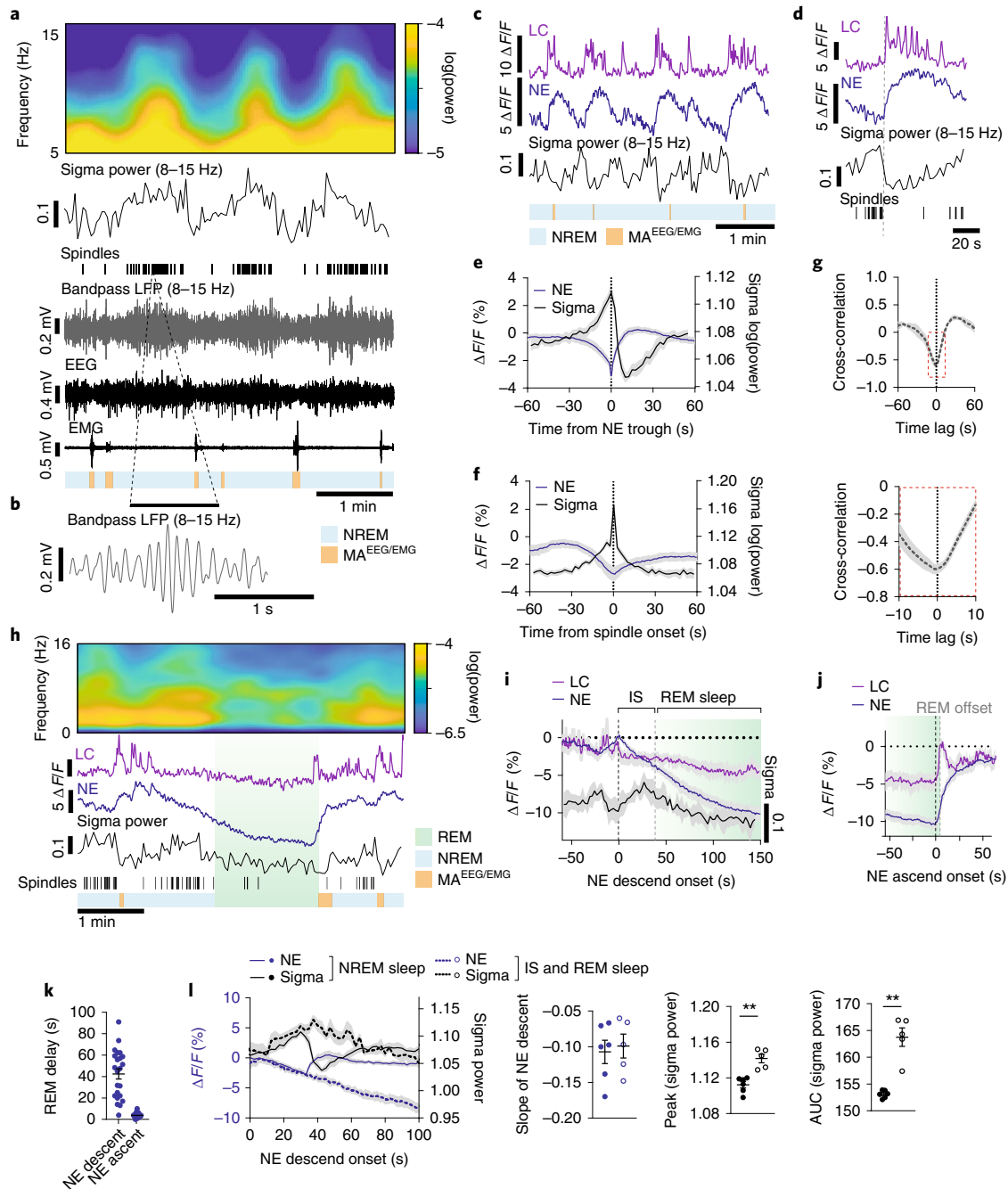
**Prolonged NE descent promotes spindle-rich IS and REM sleep transitions.** Next, we investigated how the infraslow NE oscillations shaped the occurrence of sleep spindles. Sleep spindles, characterized as short bursts (1–2 seconds) of sigma activity (8–15-Hz oscillations), have been implicated in memory consolidation<sup>2</sup>, and LC activity has been reported to terminate sleep spindle activity<sup>11,21,22,24</sup>. First, we confirmed that sigma power—the 8–15-Hz spectral power of surface EEG (5-second windows)—is a good estimate for spindle occurrences (Fig. 2a,b). We used cortical local field potential (LFP) recordings to detect spindles and compared them to sigma power obtained from simultaneous EEG recordings. LFP-detected spindle occurrences paralleled EEG sigma power and revealed infraslow sigma power oscillations across NREM sleep (Fig. 2a,b and Extended Data Fig. 3a–c), with an inverse relationship to the NE

**Fig. 1 | Increased NE descent amplitude primes awakenings over micro-arousals.** **a**, GRAB<sub>NE2m</sub> and GCaMP6f were expressed in the mPFC and LC, respectively, for combined NE and LC Ca<sup>2+</sup> measurements alongside EEG and EMG recordings. **b**, Representative traces of simultaneous recordings with EEG-scored sleep stages. **c**, Terminology used to describe NE oscillations. **d**, Mean NE oscillation frequency and amplitude during NREM and REM sleep (two-tailed paired *t*-test, *P* = 0.020). **e**, Representative traces showing NREM-related NE events associated with micro-arousals accompanied only by EEG and not EMG changes (MA<sup>NE</sup>), EEG/EMG-defined micro-arousals (MA<sup>EEG/EMG</sup>) or waking. **f**, Percentage of state transition outcome from each NE period. **g**, Mean LC traces aligned to onset of NE ascent. **h**, Zoom-in of mean LC traces (red dotted square in **g**). **i**, Amplitude of LC responses across all state transitions (two-tailed paired *t*-test: *P* = 0.09, MA<sup>NE</sup> versus MA<sup>EEG/EMG</sup>; *P* = 0.02, MA<sup>NE</sup> versus wake; *P* = 0.04, MA<sup>EEG/EMG</sup> versus wake). **j**, Mean NE traces aligned to onset of NE rise at behavioral transitions. **k–n**, Mean slope of NE descent (two-tailed paired *t*-test: *P* = 0.55, NREM versus MA<sup>EEG/EMG</sup>; *P* = 0.20, NREM versus wake; *P* = 0.19, MA<sup>EEG/EMG</sup> versus wake); NE descent time (two-tailed paired *t*-test: *P* = 0.58, MA<sup>NE</sup> versus MA<sup>EEG/EMG</sup>; *P* = 0.015, MA<sup>NE</sup> versus wake; *P* = 0.0051, MA<sup>EEG/EMG</sup> versus wake); NE trough level (two-tailed paired *t*-test: *P* = 0.22, MA<sup>NE</sup> versus MA<sup>EEG/EMG</sup>; *P* = 0.032, MA<sup>NE</sup> versus wake; *P* = 0.049, MA<sup>EEG/EMG</sup> versus wake); and NE ascent amplitude before transitions (two-tailed paired *t*-test: *P* = 0.0068, MA<sup>NE</sup> versus MA<sup>EEG/EMG</sup>; *P* = 0.0021, MA<sup>NE</sup> versus wake; *P* = 0.0022, MA<sup>EEG/EMG</sup> versus wake). **o**, Another batch of animals was exposed to tones during sleep-wake behavior, and GRAB<sub>NE2m</sub> fluorescence was measured as shown in representative trace. Tones during NREM sleep were divided into outcome (sleep or arousal). **p**, Mean NE traces related to tone onset. **q,r**, NE trough level (two-tailed paired *t*-test, *P* = 0.048) and ascent amplitude (two-tailed paired *t*-test, *P* = 0.025) at tone-induced sleep versus arousal. **s**, NE trough levels before each tone were classified as low or high (above or below mean NE trough value before all tones), and wakeup rate is shown for each group (two-tailed paired *t*-test, *P* = 0.043). **t**, Schematic summarizing our two main findings on the role of NE in sleep micro-architecture: (1) regular NE oscillations dictate micro-arousals; and (2) longer periods of NE descent associate with increased probability of awakening. **d–n**, *n* = 7; **o–s**: *n* = 6. Data are shown as mean ± s.e.m. \**P* < 0.05, \*\**P* < 0.01, \*\*\**P* < 0.001.

oscillations (Fig. 2c). Specifically, spindle occurrences (and corresponding sigma power) build up as NE descends and are terminated as NE starts to ascend (Fig. 2d and Extended Data Fig. 3d). The inverse relationship was also apparent from the peak in sigma power when assessed at times of NE troughs (Fig. 2e) and from the NE

trough occurring at points of spindle onset (Fig. 2f). Spindle onset correlated with a peak in sigma power (Fig. 2f), indicating, again, that sigma power is a good estimate of spindles. Cross-correlation analysis showed a clear inverse correlation between NE and sigma power across the recording (Fig. 2g), but causality could not be





**Fig. 2 | Prolonged NE descent promotes spindle-rich IS and REM sleep transitions.** **a**, Representative simultaneous surface EEG and depth LFP recordings showing the correlation between LFP-based spindle detection and EEG-based sigma power. Displayed are EEG power spectrogram, EEG-based sigma power, LFP-based spindle occurrences, 8-15-Hz bandpass-filtered LFP, raw EEG and EMG and color-coded sleep phases. **b**, Zoom-in of 8-15-Hz bandpass-filtered LFP showing a representative spindle. **c**, Representative traces from simultaneous measurements of LC and NE during NREM sleep and their association with sigma power. **d**, Representative LC and NE traces as well as sigma power and spindle occurrences upon NE ascent. **e**, Mean NE and sigma power traces aligned to NE trough during NREM sleep. **f**, Mean NE and sigma power traces aligned to spindle onset during NREM sleep. **g**, Cross-correlation between sigma power and NE level based on 10-minute NREM sleep epochs. Bottom: zoom-in to illustrate time lag. **h**, Representative recordings covering REM sleep transitions (REM sleep, >150 seconds in duration) showing EEG power spectrogram, LC and NE traces, sigma power, spindle occurrences and color-coded sleep phases. **i**, Mean LC and NE activity and sigma power from NE descent onset preceding REM onset. Mean onset of REM sleep is displayed. The period from NE descent onset until REM sleep onset is marked as IS sleep. **j**, Mean LC and NE activity during REM sleep aligned to the onset of NE ascent preceding REM sleep offset. Mean REM sleep offset is marked. **k**, Mean delay from NE descent onset to REM sleep onset and from NE ascent to REM sleep offset (23 REM sleep occurrences across  $n=5$ ). **l**, Mean NE and sigma power during NREM sleep versus IS-REM sleep from the onset of NE descent; slope of NE descent for NREM and IS sleep (two-tailed paired  $t$ -test,  $P=0.89$ ); increase in sigma power peak (two-tailed paired  $t$ -test,  $P=0.006$ ) and area under the curve (AUC) (two-tailed paired  $t$ -test,  $P=0.005$ ) NREM and IS-REM sleep. Significance was calculated by means of paired  $t$ -test.  $n=6$  (NREM) and  $n=5$  (IS-REM). Data are shown as mean  $\pm$  s.e.m.  $^{**}P < 0.01$ .



inferred from the cross-correlogram alone due to the broad peak. We, therefore, analyzed the temporal relationship between NE level and spindles after optogenetic activation of LC and demonstrated a time delay between NE ascent and termination of spindles, which further supports the idea that spindle occurrences depend on NE levels (Extended Data Fig. 3f). Because delta-rich NREM sleep phases are important for the restorative functions of sleep, we also performed cross-correlation analysis between delta power and NE level, but we did not find an obvious temporal association (Extended Data Fig. 3e). In summary, the infraslow oscillations of NE during NREM sleep strongly correlated with a repeated pattern of alternations between sleep spindles and micro-arousals.

Studies have reported that LC firing stops during REM sleep<sup>11,16</sup>, and, interestingly, REM sleep is always preceded by spindle-rich IS sleep<sup>29</sup>. Our observations above suggest that IS sleep occurs when the level of NE is already low. However, it is not known whether LC-NE activity is responsible for the transitioning and fixed sequential order of IS and REM sleep. We observed that, before REM sleep onset, phasic LC events ceased, initiating a continuous descent of NE levels accompanied by spindle buildup that dropped upon REM sleep entry (Fig. 2h,i). Remarkably, the NE descent before REM sleep started almost 40 seconds ( $42.3 \pm 3.8$  seconds) before REM sleep onset (Fig. 2i,k), suggesting that spindle-rich IS sleep is driven by NE descent. Interestingly, the slope of the NE descent was similar between NREM and IS sleep (Fig. 2l), indicating that the subsequent occurrence or absence of a micro-arousal is the main determinant of whether NREM sleep continues or transitions into REM sleep. Furthermore, the overall spindle occurrences (estimated by sigma power) associated with IS sleep was higher than during other phases of NREM sleep (Fig. 2l), adding additional support to the importance of IS-to-REM sleep transitions in spindle-dependent memory processes. As expected, NE continued to descend during REM sleep (Fig. 2h,i). At the offset of REM sleep, LC exhibited phasic activity accompanied by a rapid ascent in NE (Fig. 2j), with a mean delay from onset of NE increase to REM sleep offset of only ~5 seconds ( $4.7 \pm 0.5$  seconds; Fig. 2k). This analysis shows that the sequential order of spindle-rich IS and REM sleep coincide with silence of LC and a continuous descent in cortical NE levels.

**Optogenetic LC suppression induces IS-REM sleep sequences and improves memory.** To assess the causal role of NE oscillations on memory performance, we sought to increase the amplitude of NE descent in a time-specific manner by periodic optogenetic inhibition. We expressed the light-driven proton pump Arch-eGFP or eYFP-only construct bilaterally in LC TH-positive neurons and delivered continuous green (532 nm, 2.5 mW in each hemisphere) light to LC for 2 minutes every 10 minutes while recording mPFC GRAB<sub>NE2m</sub> fluorescence, EEG and EMG (Fig. 3a,b and Extended Data Fig. 4a,b). The inhibitory effect of Arch stimulation has been questioned<sup>30</sup>, and even though we did not directly assess the effect of Arch stimulation on LC cell firing, we were able to demonstrate a steady descent in NE levels during NREM sleep (Fig. 3c,d) after stimulation of Arch-expressing LC cells. The NE descent was accompanied by buildup in sigma power, peaking after ~40 seconds (Fig. 3c,d and Extended Data Fig. 4c). The amount of sigma power correlated with the degree of NE descent (Fig. 3e). This suggests that low NE plays a permissive role in sleep spindle generation.

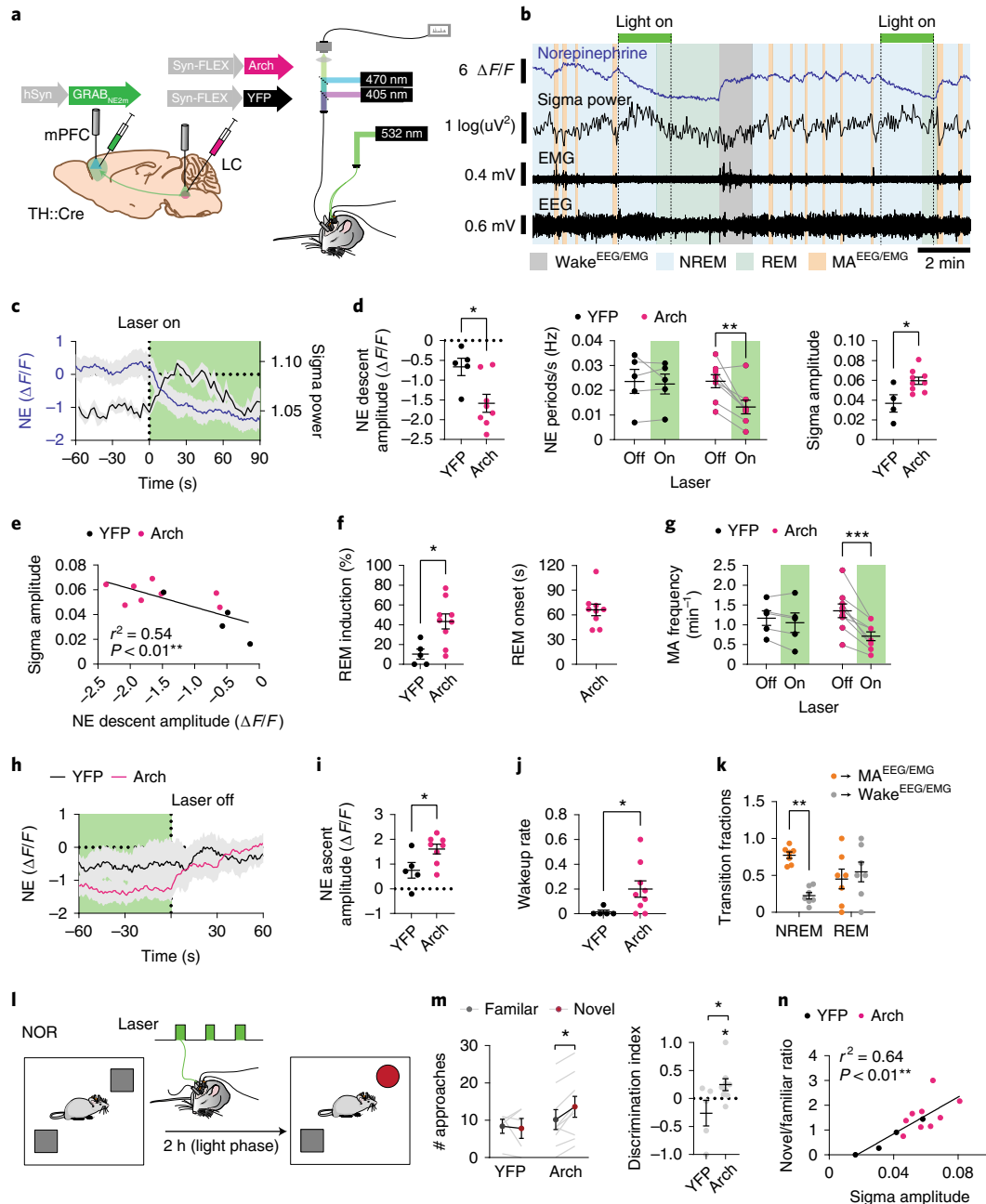
Next, we asked if enhancing the amplitude of NE descent would facilitate spindle-rich IS and REM sleep transition. Indeed, optogenetic suppression of LC activity substantially increased the probability of transitioning into REM sleep, with an average delay of  $66.1 \pm 7.0$  seconds (mean  $\pm$  s.e.m.) from laser stimulation to REM sleep onset (Fig. 3f). The ~65-second delay corresponds to the time-point when sigma power returns to baseline (Fig. 3c) and aligns with the observation that 40-second NE descent precedes REM

sleep onset during normal conditions (Fig. 2h-k). Additionally, the prolonged elevation of sigma power mimicked sigma increases observed in IS-REM sleep transitions (Extended Data Fig. 4d). Thus, these observations suggest that suppression of LC activity and continuous NE descent induces sleep stages similar to the sequentially linked IS and REM sleep.

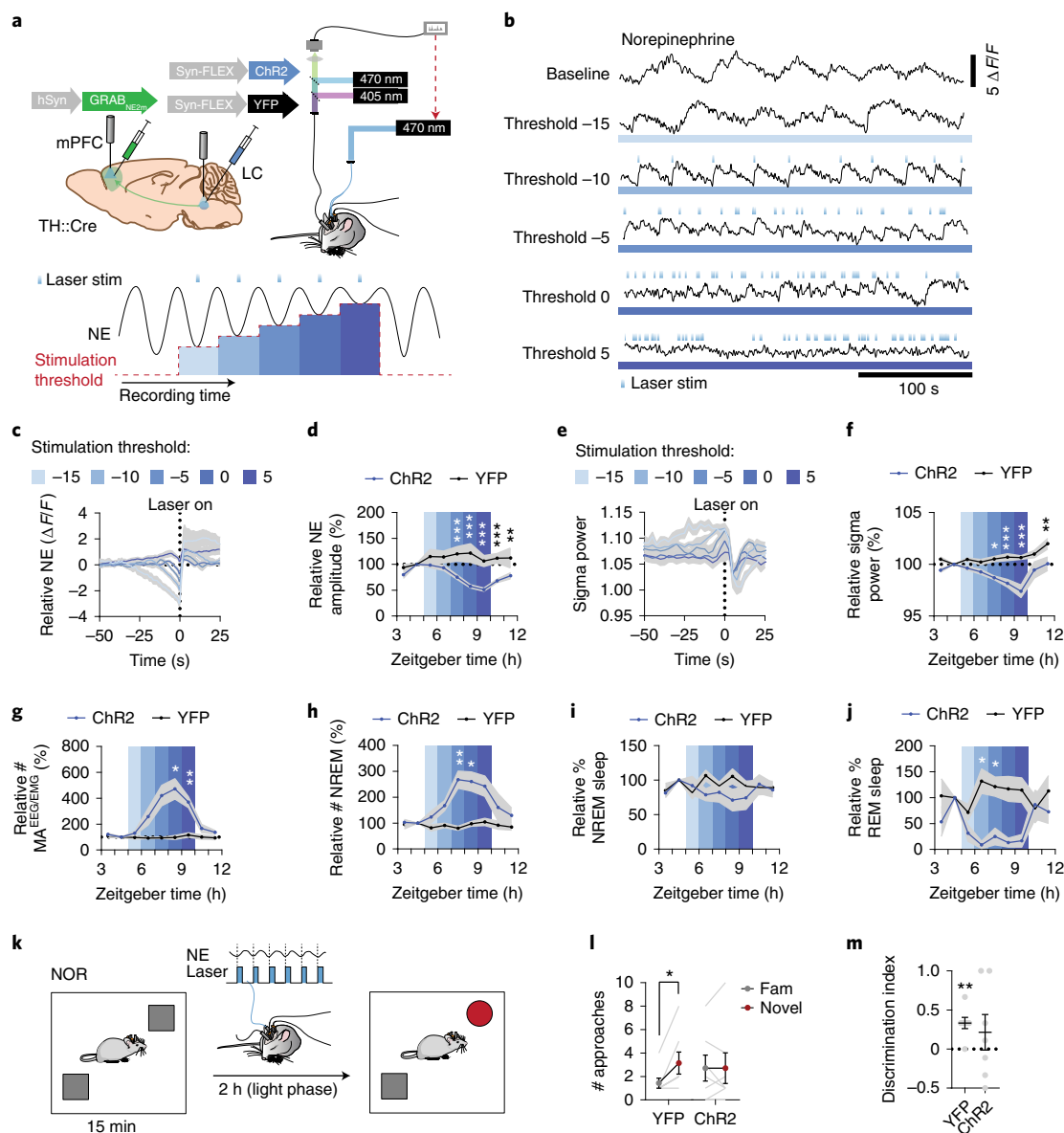
Then, we examined if the induction of NE descent increased the probability of awakening once LC was released from inhibition. Although the rate of micro-arousals decreased during optogenetic suppression of LC (Fig. 3g), once the laser was turned off the subsequent NE ascents (Fig. 3h,i) were associated with a higher rate of awakenings compared to control animals (Fig. 3j), confirming the prior observation that longer periods of NE descent enhance the likelihood of awakening (Fig. 1j). However, termination of light-induced Arch stimulation has been associated with rebound excitation activity, which potentially confounds this observation<sup>31,32</sup>. We, therefore, assessed natural REM sleep incidents, where NE has remained low for an extended period; this revealed that around half of REM sleep offsets are characterized by an awakening, whereas micro-arousals are more prevalent than awakenings at NREM sleep offset (Fig. 3k). Thus, enhanced NE descent amplitude may prime the animals toward awakening.

Finally, we examined the effects of LC optogenetic suppression on memory performance. The animals were subjected to the novel object recognition task and afterwards left to sleep between the encoding and recall phase of the task while stimulated with laser for 2 minutes every 6 minutes (Fig. 3l). Animals were well-habituated to the resting cages and were mainly asleep during the stimulation period, and most stimulations occurred during NREM sleep (Extended Data Fig. 4e,f). The stimulations that occurred during wakefulness did not have a significant effect on NE levels or induction of NREM sleep (Extended Data Fig. 4g-i). The LC suppression paradigm increased preference toward the novel objects compared to YFP controls, without affecting the movement of the animal (Fig. 3m and Extended Data Fig. 4j,k). The preference toward the novel objects correlated strongly with the amount of sigma power induced by the NE suppression (Fig. 3n) but not with duration, bout number or theta power of REM sleep, nor did it correlate with NREM sleep duration or with the amplitude of theta or delta power during laser stimulations (Extended Data Fig. 4l-q). Thus, enhancing NE descent amplitude by regular LC optogenetic inhibition induces spindle-rich IS-REM sleep sequences and promotes memory performance.

**Optogenetic reduction of NE amplitude reduces spindles and disrupts memory performance.** To reduce the amplitude of NE oscillations in a sleep-phase-specific manner, we performed NE descent-dependent optogenetic activation of LC. We expressed the light-activated cation channel channelrhodopsin-2 (ChR2) bilaterally in TH-positive LC neurons and GRAB<sub>NE2m</sub> in mPFC neurons while implanting screws for EEG and EMG measurements (Fig. 4a). NE level ( $\Delta F/F$  (%)) was calculated in real time, and crossing of lower NE threshold values was used to trigger fast optogenetic stimulation of LC (2 seconds, 20 Hz, 10-ms blue light pulses). After habituation, the experiment started with a 2-hour baseline recording after which threshold-based activation was initiated. The threshold was subsequently lifted in increments of 5  $\Delta F/F$  (%) every hour (from -15 to 5  $\Delta F/F$  (%)), followed by 2 hours of stimulation-free recording (Fig. 4a). The stimulation paradigm resulted in a gradual decrease in NE descent amplitude over the course of the stimulation thresholds (Fig. 4b-d) with corresponding reductions in sigma power (Fig. 4e,f) and increases in micro-arousal occurrences (Fig. 4g). This resulted in an increasingly fragmented NREM sleep pattern (Fig. 4h) without affecting the overall duration of NREM sleep (Fig. 4i). Of note, REM sleep duration was significantly decreased by LC activation even at low threshold values (Fig. 4j).



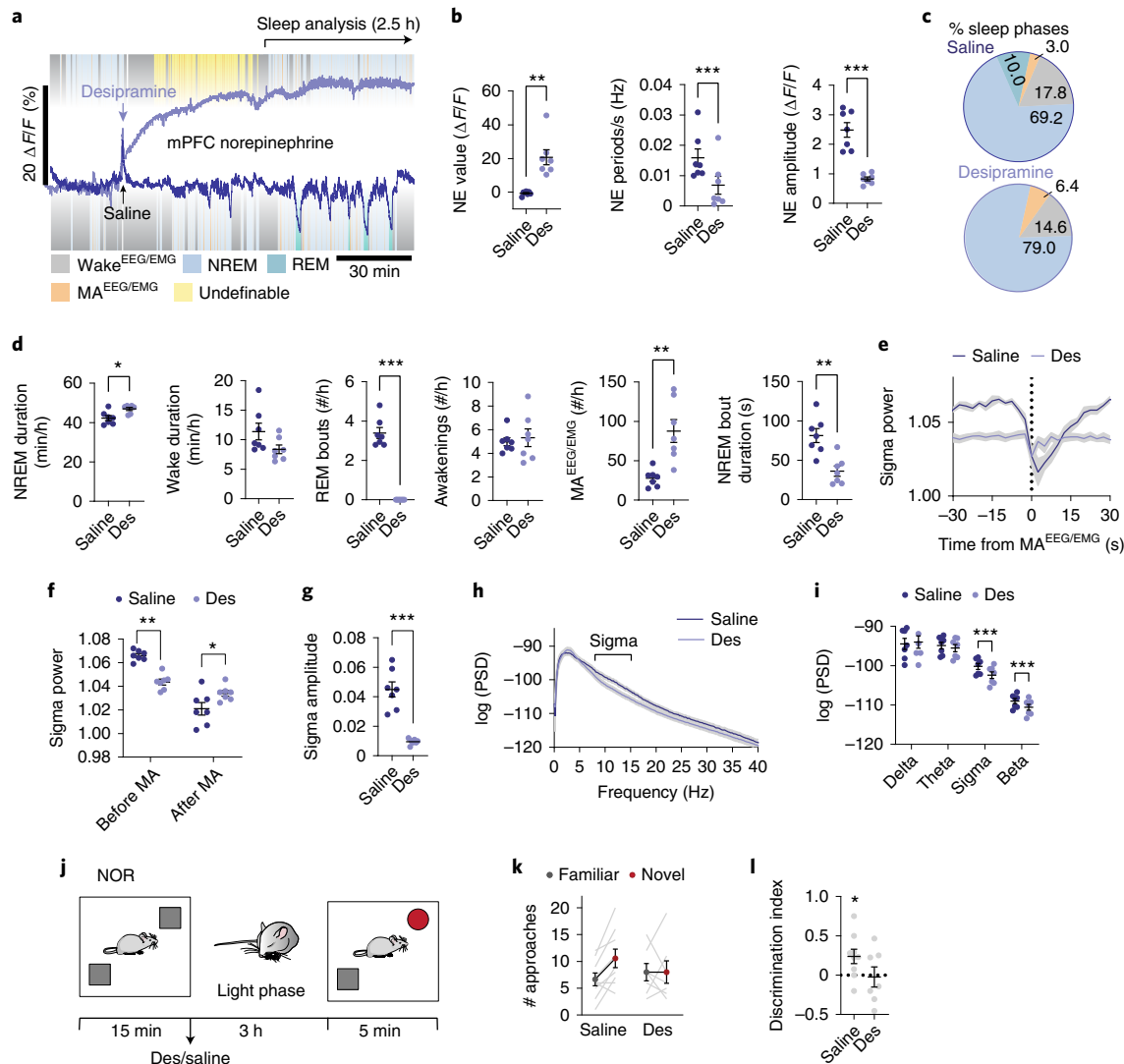
**Fig. 3 | Optogenetic suppression of LC induces IS-REM sleep sequences and improves memory.** **a**, Arch was expressed in LC, and GRAB<sub>NE2m</sub> was expressed in mPFC. Green laser light was delivered to LC during combined fiber photometry and EEG/EMG recordings. **b**, Example traces showing the effects of 2-minute optogenetic suppression of LC on NE levels and sigma power. **c**, Mean NE and sigma power traces aligned to laser stimulation onset in Arch-expressing animals. **d**, NE descent amplitude induced by laser onset during NREM sleep (left) (two-tailed unpaired *t*-test,  $P=0.020$ ), NE oscillation frequency for laser-off and laser-on periods (middle) (two-way repeated-measures ANOVA with Sidak's multiple comparison post hoc test:  $P=0.92$ , YFP;  $P=0.0016$ , Arch) and mean amplitude of sigma response after laser onset (right) (two-tailed unpaired *t*-test,  $P=0.015$ ). **e**, Correlation between sigma amplitude and NE change in response to laser stimulation (linear regression). **f**, Percentage of 2-minute laser stimulations resulting in REM transition (left) (two-tailed unpaired *t*-test,  $P=0.011$ ). Mean time from laser onset before REM onset (right). **g**, Frequency of EEG/EMG-defined micro-arousals (MAs) during optogenetic LC suppression (two-way repeated-measures ANOVA with Sidak's multiple comparison post hoc test:  $P=0.60$ , YFP;  $P<0.0001$ , Arch). **h**, Mean NE traces aligned to laser stimulation offset. **i**, NE ascent amplitude after laser offset (two-tailed unpaired *t*-test,  $P=0.033$ ). **j**, The wakeup rate within 15 seconds of laser offset (one-tailed Mann-Whitney test,  $P=0.018$ ). **k**, Outcome of sleep termination from NREM and REM sleep (animals from Figs. 1 and 2; two-way repeated-measures ANOVA with Sidak's multiple comparison post hoc test:  $P=0.0013$ , NREM;  $P=0.75$ , REM). **l**, Animals were subjected to novel object recognition and allowed to sleep for 2 hours with laser stimulations between encoding and recall. **m**, Number of approaches to novel and familiar objects (two-way repeated-measures ANOVA with Sidak's multiple comparison post hoc test:  $P=0.91$ , YFP;  $P=0.023$ , Arch) and discrimination index (one-sample *t*-test,  $P=0.32$ , YFP;  $P=0.047$ , Arch, two-tailed unpaired *t*-test,  $P=0.038$ ). **n**, Correlation between approach ratio and mean sigma response to laser stimulations during sleep (linear regression).  $n=9$  Arch;  $n=5$  YFP. Data are shown as mean  $\pm$  s.e.m. \* $P<0.05$ , \*\* $P<0.01$ , \*\*\* $P<0.001$ . NOR, novel object recognition.



**Fig. 4 | Optogenetic reduction of NE amplitude reduces sigma activity and disrupts memory.** **a**, Top: ChR2 was expressed in LC, and GRAB<sub>NE2m</sub> was expressed in mPFC. Blue laser light was delivered to LC during combined fiber photometry and EEG/EMG recordings. Bottom: 2-hour baseline recording was followed by five periods lasting 1 hour with increasing NE thresholds for laser stimulations, followed by a 2-hour stimulation-free period. Laser stimulations were triggered when real-time  $\Delta F/F$  (%) calculations of NE levels went below the threshold. **b**, Example traces from each stimulation period are shown with triggered laser stimulations. **c**, Normalized mean NE traces leading up to laser onset for each stimulation threshold. **d**, Mean relative NE amplitude during NREM sleep across each stimulation paradigm (two-way repeated-measures ANOVA with Sidak's multiple comparison post hoc test:  $P=0.0006$ , threshold  $-5$ ;  $P<0.0001$ , threshold  $0$ ;  $P<0.0001$ , threshold  $5$ ;  $P=0.0008$ , washout 1;  $P=0.0079$ , washout 2). **e**, Mean sigma power leading up to laser stimulation for each threshold. **f**, Mean relative sigma power during NREM sleep across stimulation paradigms (two-way repeated-measures ANOVA with Sidak's multiple comparison post hoc test:  $P=0.012$ , threshold  $-5$ ;  $P=0.0001$ , threshold  $0$ ;  $P<0.0001$ , threshold  $5$ ;  $P=0.0055$ , washout 2). **g,h**, Number of micro-arousals (MA<sup>EEG/EMG</sup>) per minute spent in NREM sleep (two-way repeated-measures ANOVA with Sidak's multiple comparison post hoc test:  $P=0.028$ , threshold  $0$ ;  $P=0.0064$ , threshold  $5$ ) and NREM sleep bouts per hour (two-way repeated measures ANOVA with Sidak's multiple comparison post hoc test:  $P=0.0090$ , threshold  $-5$ ;  $P=0.037$ , threshold  $0$ ) during each stimulation paradigm. **i,j**, Percent time spent in NREM (two-way repeated-measures ANOVA with Sidak's multiple comparison post hoc test) and REM sleep (two-way repeated-measures ANOVA with Sidak's multiple comparison post hoc test:  $P=0.024$ , threshold  $-10$ ;  $P=0.025$ , threshold  $-5$ ) across stimulation paradigms. **k**, Animals were subjected to novel object recognition and stimulated using the threshold  $=0$  paradigm for 2 hours between memory encoding and recall. **l**, Number of approaches to familiar and novel objects (two-way repeated-measures ANOVA with Sidak's multiple comparison post hoc test:  $P=0.022$  YFP;  $P>0.99$ , ChR2). **m**, Discrimination index based on number of approaches (one-sample  $t$ -test:  $P=0.0038$ , YFP;  $P=0.38$ , ChR2; two-tailed unpaired  $t$ -test,  $P=0.63$ ).  $n=7$  ChR2;  $n=7$  YFP. Data are shown as mean  $\pm$  s.e.m. \* $P<0.05$ , \*\* $P<0.01$ , \*\*\* $P<0.001$ . NOR, novel object recognition.

To investigate if induction of a sleep pattern characterized by low NE oscillatory amplitude and reduced spindle activity would affect memory performance, we again subjected animals to novel object

recognition and stimulated mice with the threshold  $0$  setting for 2 hours between memory encoding and recall (Fig. 4k). Animals in the ChR2 group did not show a preference for the novel object over



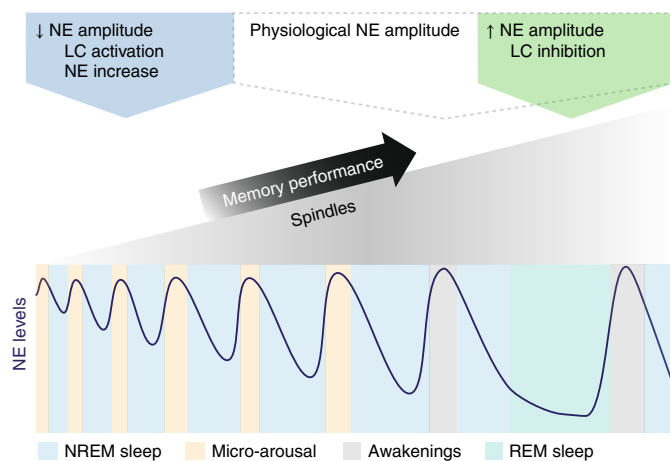
**Fig. 5 | Pharmacological reduction of NE amplitude promotes micro-arousal and compromises memory.** **a**, Mice were administered with saline or desipramine (Des, 10 mg kg<sup>-1</sup>, intraperitoneal) during the light phase and allowed to sleep for 3.5 hours. Three days after, treatment was reversed. Analysis was done on a 1–3.5-hour period after administration. **b**, Effect of desipramine on mean NE value (two-tailed paired *t*-test,  $P=0.0026$ ), NE oscillation frequency (two-tailed paired *t*-test,  $P=0.0004$ ) and NE amplitude during NREM sleep (two-tailed paired *t*-test,  $P=0.0003$ ). **c**, Mean distribution of % time spent in NREM sleep, REM sleep, wakefulness and micro-arousals. **d**, Time spent in NREM sleep (two-tailed paired *t*-test,  $P=0.030$ ) and wake (two-tailed paired *t*-test,  $P=0.64$ ), number of REM bouts (two-tailed paired *t*-test,  $P<0.0001$ ), wake bouts (two-tailed paired *t*-test,  $P=0.70$ ), micro-arousals (two-tailed paired *t*-test,  $P=0.0041$ ) and mean duration of NREM sleep bouts (two-tailed paired *t*-test,  $P=0.0029$ ). **e**, Mean sigma power traces aligned to NREM-to-MA<sup>EEG/EMG</sup> transition. **f**, Mean sigma power before and after NREM-to-MA<sup>EEG/EMG</sup> transition (two-way repeated-measures ANOVA with Sidak's multiple comparison post hoc test:  $P=0.0024$ , before, and  $P=0.031$ , after). **g**, Mean sigma power amplitude reduction across NREM-to-MA<sup>EEG/EMG</sup> transition (two-tailed paired *t*-test,  $P=0.0007$ ). **h, i**, Power spectral densities during NREM sleep and mean power spectral densities across frequency bands (two-way repeated-measures ANOVA with Sidak's multiple comparison post hoc test:  $P=0.72$ , delta;  $P=0.10$ , alpha;  $P=0.0003$ , sigma;  $P<0.0001$ , beta). **j**, In a separate experiment, mice were subjected to novel object recognition (NOR) during their light phase and administered with desipramine or saline immediately after the encoding phase. Mice were allowed to sleep for 3 hours before the recall phase. **k**, Number of approaches toward novel versus familiar object during recall. **l**, Discrimination index for novel versus familiar object (one-sample *t*-test:  $P=0.032$ , saline, and  $P=0.86$ , Des; two-tailed unpaired *t*-test,  $P=0.11$ ).  $n=7$  (**a–i**),  $n=7$  Des,  $n=9$  saline (**j–l**). Data are shown as mean  $\pm$  s.e.m. \* $P<0.05$ , \*\* $P<0.01$ , \*\*\* $P<0.001$ . MA, micro-arousal; PSD, power spectral density.

the familiar object, unlike animals in the YFP control group, which was not explained by a difference in locomotion during the acquisition or recall phase (Fig. 4l,m and Extended Data Fig. 5).

Overall, these findings confirm the key role of NE oscillations in shaping sleep micro-architecture important for memory consolidation and suggest that NE amplitude controls the switch between micro-arousal-interspersed NREM sleep and memory-enhancing IS-REM sleep sequences.

**Pharmacological reduction of NE amplitude promotes micro-arousals and compromises memory.** Our findings suggest that therapeutic treatment based on elevation of NE can lead to altered sleep structure and memory deficits by reducing the amplitude of NE oscillations. Interestingly, antidepressant treatment involving NE re-uptake inhibition has been linked to reduced LC responsiveness<sup>33</sup>, sedation and REM sleep suppression but also to sleep disruption<sup>34–36</sup>. To test the postulate that elevated NE will compromise





**Fig. 6 | Model diagram: NE amplitude defines the memory restorative properties of sleep.** This diagram depicts NE amplitude changes during normal sleep micro-architecture and LC-NE manipulations: Sleep is characterized by infraslow  $\sim 0.02$ -Hz NE oscillations, and the oscillatory amplitude determines both behavioral arousal and the amount of sleep spindles and spindle-rich IS-REM sleep sequences. Reducing NE oscillation amplitude by NE re-uptake inhibition or optogenetic activation increases micro-arousals at the cost of spindle-rich sleep needed for memory consolidation. In contrast, augmenting NE amplitude by optogenetic inhibition favors a sleep composition with more frequent spindle-rich IS and REM sleep transitions, resulting in improved memory performance despite increased incidents of awakenings.

sleep micro-structure through reduced NE dynamics, we administered the NE re-uptake inhibitor desipramine ( $10 \text{ mg kg}^{-1}$ ) and evaluated the effect on sleep starting 1 hour after administration. Desipramine increased the NE baseline value 20-fold and abolished the infraslow NE oscillatory activity during NREM sleep, as shown by reduced NE oscillation frequency and NE amplitude (Fig. 5a,b). Desipramine also altered the sleep pattern (Fig. 5c), with increased NREM sleep and total elimination of REM sleep (Fig. 5c,d and Extended Data Fig. 6a,b). This observation provides support for the permissive effect of NE descent on REM sleep onset but contradicts the concept that high NE promotes awakening, as could be expected from previous literature<sup>15,34,37</sup>. Furthermore, the resulting NREM sleep was characterized by an increased amount of  $\text{MA}^{\text{EEG/EMG}}$  (Fig. 5d); intriguingly, however, both  $\text{MA}^{\text{EEG/EMG}}$ -induced arousability and  $\text{wake}^{\text{EEG/EMG}}$ -induced arousability (defined as reductions in sigma power; Extended Data Fig. 1) were substantially decreased and shortened (Fig. 5e–g and Extended Data Fig. 6c–e). These observations support the idea that NE amplitude, rather than absolute NE levels, is important for micro-arousal and wake transitioning and that reducing the amplitude of NE oscillations leads to less defined brain state transitions. It also corroborates our finding that lower NE descent amplitude primes micro-arousals over awakenings (Fig. 1j–l). Furthermore, power spectral analysis revealed reduced EEG power in the sigma and beta range during NREM sleep but no change in delta and theta bands (Fig. 5h,i and Extended Data Fig. 6a,b). Reduced sigma power corresponds to a lower occurrence of spindles, suggesting an inverse relationship between NE and spindles. The combination of reduced spindle occurrences and abolished REM sleep transitions suggests that constant elevation of NE compromises spindle-enriched IS-REM sleep transitions. To determine if these sleep changes had any effect on memory performance, a separate batch of mice was given desipramine or saline immediately after the encoding phase of the novel object recognition task and allowed to sleep for 3 hours (Fig. 5j). During the recall phase, assessing the number of approaches toward the two objects

(Fig. 5k) revealed that saline-administered animals preferred the novel object, whereas the desipramine-treated animal did not show any preferences (Fig. 5l). The movement of the animals during the recall phase was similar, as was the movement and object exploration during the drug-free acquisition phase (Extended Data Fig. 6f). Thus, desipramine administration reduces the memory performance of the animals without affecting the general activity level of the mice. These results show that drug-induced elevation of NE suppresses sleep micro-structures governed by the infraslow NE oscillations, which compromises memory-promoting segments of sleep.

Taken together, we show that  $\sim 0.03$ -Hz NE oscillations during sleep drive periodic micro-arousals, whereas longer descents raise the probability of awakening. Increasing oscillation amplitudes allows for increased sleep spindle activity, which supports memory performance and is associated with IS-to-REM sleep transition (Fig. 6). By contrast, lowering NE oscillation amplitude by optogenetic or pharmacologic intervention increases micro-arousals and sleep fragmentation, suppresses sleep-spindle activity, and consequently impairs memory performance.

## Discussion

It is widely accepted that spindles and REM sleep are important for memory-enhancing aspects of sleep, and excessive fragmentation of sleep negatively affects daytime performance<sup>5,38,39</sup>. However, the neural mechanisms orchestrating naturally occurring sleep-fragmenting elements, such as micro-arousals and awakenings and their interrelationship to the memory-enhancing segments of sleep, are unknown. Real-time assessment of NE levels by fiber photometry allowed us to dissect the role of NE in sleep micro-architecture with a time resolution of seconds. We found that phasic bouts of LC activity (every  $\sim 30$  seconds) during NREM sleep generate infraslow oscillations of cortical NE levels that drive micro-arousals and subdivide sleep into microstructures important for memory consolidation. The analysis reveals that the oscillation amplitude of NE during NREM sleep determines the memory restorative quality of sleep; reducing or increasing NE oscillatory amplitude either compromises or improves memory performance after sleep. These new observations extend the current view of NE as a neuromodulator that governs macroscale brain states<sup>18,19</sup> to include sleep micro-architecture.

The general thought has been that LC reduces its tonic activity during sleep<sup>11,13,14,16,17</sup> with a subsequent overall reduction in NE levels<sup>18,19</sup>. However, we now demonstrate that the NE levels during sleep oscillate in an infraslow manner with a periodicity of  $\sim 30$  seconds created by the alternation between LC silence and phasic LC activity. Intriguingly, the LC phasic activity behind the infraslow NE oscillations consistently drives micro-arousals during the NE ascending state. Thus, we unveil a novel mechanism behind spontaneously occurring micro-arousals and demonstrate that micro-arousals are not generated at random during NREM sleep but follow the cyclic nature of LC activations. It is important to note that LC is one of several reciprocally interconnected arousal-promoting systems in the brain that include cholinergic, serotonergic, histaminergic, and dopaminergic nuclei, collectively known as the ascending reticular activating system<sup>40</sup>. Therefore, it is likely that all these neuromodulators would exhibit increases during micro-arousals; however, our demonstration that optogenetic suppression of LC reduces the appearance of micro-arousals indicates that LC is particularly important for the initiation of micro-arousals. Because these periodic LC activations during sleep have not, to our knowledge, been described before, we can only speculate on their origin, but anatomical tracing studies show prominent inputs to LC from medullary nuclei<sup>41,42</sup>, indicating a tight connection to the autonomic system<sup>43,44</sup>.

After finding that ascending phases of the infraslow NE oscillations drive micro-arousals, we were interested in determining the

effect of the descending phase on sleep processes. Previous studies showed that the LC-NE system is involved in the termination of sleep spindles; single-unit recordings demonstrate that LC firing correlates with the discontinuation of spindles<sup>11,21,22</sup>. We show here that the LC-NE system is also involved in the generation of spindles. It is the steady descent of NE that is responsible for buildup of spindles; the amount of NE descent correlates with the amount of spindle activity, and NE ascents abruptly terminate this activity. Thus, the infraslow NE oscillations during NREM sleep drive coherent periodic fluctuations in spindle activity, creating distinct spindle-rich sleep structures. The existence of infraslow sigma power fluctuations has been documented in both mice and humans<sup>23</sup>, although the primary drive of the oscillations has remained unknown until now<sup>24</sup>.

We were interested in determining whether increasing NE oscillatory descent amplitude could increase the amount of spindle buildup during NREM sleep. IS sleep is a well-defined NREM sleep stage that occurs before REM sleep onset and is characterized by particularly high spindle activity<sup>29,45</sup>. Our analysis demonstrates that the spindle-rich IS sleep is associated with larger descent amplitude of NE compared to remaining NREM sleep. Namely, ~40 seconds before REM sleep, NE starts to descend, which allows enriched buildup of spindle activity. At REM sleep transitioning, spindles are not abruptly terminated but slowly start to subside, likely due to activation of the pedunculopontine nuclei that promotes acetylcholine release and REM sleep transitioning while suppressing spindle activity through parallel projections to the cholinergic basal forebrain and thalamus<sup>40,46</sup>. The overall induction of spindles is larger for the IS-REM sleep sequence compared to the shorter-lasting spindle increases interspersed within NREM sleep.

It is well-established that NE levels are lower during REM sleep than during NREM sleep<sup>18,19</sup>, and, indeed, NE exhibits a continuous descent during REM sleep in addition to the 40-second decrease before episode onset. The linear descent in NE suggests complete silence of LC activity during and before REM sleep, which is also apparent from the lack of LC activity. Furthermore, we show that low NE is a requirement of REM sleep induction. The necessity of low LC-NE activity for REM sleep induction is supported by several studies<sup>47,48</sup>, likely through the permissive effect of low NE on activation of the pedunculopontine nuclei<sup>49</sup>, although controversies exist<sup>15,20</sup>.

Both sleep spindles and REM sleep are implicated in memory consolidation processes<sup>1,2,50,51</sup>. If pronounced NE descents are associated with higher spindle incidents during IS-REM sleep transitions, larger NE oscillatory amplitudes may be particularly important for memory performance. To increase NE oscillatory amplitude, we optogenetically silenced the LC during sleep at regular intervals. This intervention led to buildup of spindle activity and induced sleep sequences resembling IS and REM sleep (Fig. 3). Remarkably, we could enhance memory performance; a strong correlation between the induced spindle activity and subsequent memory performance for the individual animals was evident when LC was silenced. It has been hypothesized that the sequential order of IS and REM sleep serves an important function, where memory representations tagged by spindles are further processed during REM sleep<sup>32,53</sup>. Neither duration nor frequency of REM sleep correlated with individual behavioral performances, indicating that spindle-rich IS sleep might be a better marker for memory performance. In support of these findings, pharmacological and optogenetic elevation of NE abolishing NE oscillations resulted in expression of spindle-poor NREM sleep and elimination of IS-to-REM sleep transitions and compromised memory performance. These findings support previous studies demonstrating that optogenetic or electrical activation of LC during sleep disrupts spindle generation and reduces memory performance<sup>22,25</sup>, which we ascribe to abolishment of NE oscillations. Although NE re-uptake inhibition has been demonstrated to

reduce spindle-dependent memory<sup>36</sup>, other studies show that this treatment increases memory performance<sup>34,55</sup>. However, the latter studies did not show upregulation of NE levels, which may explain the discrepancies. Furthermore, the effects on sleep of systemic elevation of NE is complex, as it can involve multiple neuromodulator systems and receptor targeting<sup>34,35</sup>. Our results pinpoint the need for future therapeutic strategies focusing on maintaining NE oscillation amplitude and intact sleep micro-architecture. The data presented here suggest that treatment focusing on enhancing NE oscillations might provide a powerful therapeutic tool in promoting the memory-enhancing segments of sleep.

Although it is unlikely that awakening directly benefits memory consolidation, we observed that increased awakenings is an integral part of higher NE oscillation amplitude and IS-REM sleep sequences. Thus, our observations may suggest that the full consolidation potential of normal sleep is not exploited due to the prevalence of infraslow NE oscillations keeping its amplitude to a level that upholds mainly NREM sleep in exchange for IS-REM sleep sequences and awakenings. Furthermore, our observations may explain why excessive micro-arousals have previously been associated with performance reductions<sup>5-7</sup>. We show that gradually increasing the number of micro-arousals through NE threshold-based LC optogenetic activation reduces the oscillatory amplitude of NE needed for spindle buildup in a titrated manner that leads to an overall reduction in spindles and memory consolidation (Fig. 4). An interesting consideration is that micro-arousals and awakenings are, by nature, sleep-fragmenting events, which are, in general, considered detrimental to memory performance. However, our results suggest that this interpretation should be revisited and that the effect on memory consolidation depends on the sleep micro-architecture associated with the sleep fragmentation. Thus, awakenings are more strongly linked to IS-REM sleep transitions than micro-arousals.

If low NE levels are a prerequisite for spindle induction and memory performance, why are intrinsic LC-NE-driven micro-arousals such an inherent part of sleep? It is tempting to speculate that NE oscillations may serve to sustain NREM sleep through cyclic interruptions of NE descents that would otherwise lead to IS-REM sleep induction. So, what governs whether an LC activation during sleep results in a micro-arousal versus an awakening? The experimental design of this study allowed us, to our knowledge for the first time, to define how the cyclic changes in NE levels predict whether phasic LC activation results in micro-arousals or an awakening. One of the most surprising observations was that prolonged periods of natural NE descent (~40–50 seconds) increased the likelihood of awakening in response to both intrinsic and external arousal input. Furthermore, we found that REM sleep associated with longer periods of LC silence compared to NREM sleep more often results in awakenings when LC is re-activated, leading to the important notion that the relative increase in NE is a better predictor of awakening than absolute NE level. Thus, shifting NE amplitudes heavily influences the ability to mediate brain state transitions. Several studies have demonstrated that the  $\alpha_2$ -adrenergic receptor inhibits LC cell firing, and blockade of this receptor increases the excitability of LC neurons<sup>56,57</sup>. Thus, long durations of NE descent likely reduce  $\alpha_2$ -mediated inhibition and facilitates the excitability of LC neurons, which increases the propensity toward arousal. Similarly, Hayat et al.<sup>58</sup> demonstrated enhanced sound-triggered awakening during REM sleep. It is conceivable that the 30-second periodicity of LC activation during NREM sleep reflects a feedback mechanism that limits the extent of NE descent, thereby keeping LC auto-inhibition to a level that reduces the risk of awakenings and promotes micro-arousals. Hayat et al. also discovered that higher levels of tonic LC activity in sleeping rats increases sensitivity toward external stimuli<sup>58</sup>. A plausible explanation is that lowering of  $\alpha_2$ -mediated inhibition of LC neurons leads to membrane

depolarization and reduced spiking threshold, resulting in dispersed tonic LC firing. Although it is not clear how this elevation in tonic firing of LC neurons contributes to cortical NE level, a recent study shows that condensed phasic-like LC-NE axonal activity more effectively releases NE in the cortex<sup>59</sup>.

In this study, we demonstrate that infraslow NE oscillations are a key player in shaping sleep micro-architecture. Specifically, tuning down NE oscillatory amplitude favors micro-arousals, thus sustaining NREM sleep, and promoting NE descent boosts spindle occurrences associated with IS sleep but primes awakenings. It is possible that previous reports documenting compromised cognitive performance due to disturbed sleep with frequent interruptions<sup>38</sup> could be explained by a reduction in the oscillatory amplitude of NE, which reduces the restorative aspects of sleep while increasing the number of micro-arousals.

### Online content

Any methods, additional references, Nature Research reporting summaries, source data, extended data, supplementary information, acknowledgements, peer review information; details of author contributions and competing interests; and statements of data and code availability are available at <https://doi.org/10.1038/s41593-022-01102-9>.

Received: 2 August 2021; Accepted: 19 May 2022;

Published online: 07 July 2022

### References

- Andrillon, T. et al. Sleep spindles in humans: insights from intracranial EEG and unit recordings. *J. Neurosci.* **31**, 17821–17834 (2011).
- Fernandez, L. M. J. & Lüthi, A. Sleep spindles: mechanisms and functions. *Physiol. Rev.* **100**, 805–868 (2020).
- Bonnet, M. H. & Arand, D. L. EEG arousal norms by age. *J. Clin. Sleep. Med.* **3**, 271–274 (2007).
- Boselli, M., Parrino, L., Smerieri, A. & Terzano, M. G. Effect of age on EEG arousals in normal sleep. *Sleep* **21**, 351–357 (1998).
- Bonnet, M. H. Effect of sleep disruption on sleep, performance, and mood. *Sleep* **8**, 11–19 (1985).
- Rauchs, G. et al. Is there a link between sleep changes and memory in Alzheimer's disease? *Neuroreport* **19**, 1159–1162 (2008).
- Landolt, H. P., Dijk, D. J., Achermann, P. & Borbély, A. A. Effect of age on the sleep EEG: slow-wave activity and spindle frequency activity in young and middle-aged men. *Brain Res.* **738**, 205–212 (1996).
- Soltani, S. et al. Sleep–wake cycle in young and older mice. *Front. Syst. Neurosci.* **13**, 51 (2019).
- Saper, C. B., Fuller, P. M., Pedersen, N. P., Lu, J. & Scammell, T. E. Sleep state switching. *Neuron* **68**, 1023–1042 (2010).
- Constantinople, C. M. & Bruno, R. M. Effects and mechanisms of wakefulness on local cortical networks. *Neuron* **69**, 1061–1068 (2011).
- Aston-Jones, G. & Bloom, F. E. Activity of norepinephrine-containing locus coeruleus neurons in behaving rats anticipates fluctuations in the sleep–waking cycle. *J. Neurosci.* **1**, 876–886 (1981).
- Hobson, J. A., McCarley, R. W. & Wyzinski, P. W. Sleep cycle oscillation: reciprocal discharge by two brainstem neuronal groups. *Science* **189**, 55–58 (1975).
- Eschenko, O. & Sara, S. J. Learning-dependent, transient increase of activity in noradrenergic neurons of locus coeruleus during slow wave sleep in the rat: brain stem–cortex interplay for memory consolidation? *Cereb. Cortex* **18**, 2596–2603 (2008).
- Eschenko, O., Magri, C., Panzeri, S. & Sara, S. J. Noradrenergic neurons of the locus coeruleus are phase locked to cortical up–down states during sleep. *Cereb. Cortex* **22**, 426–435 (2012).
- Carter, M. E. et al. Tuning arousal with optogenetic modulation of locus coeruleus neurons. *Nat. Neurosci.* **13**, 1526–1533 (2010).
- Rasmussen, K., Morilak, D. A. & Jacobs, B. L. Single unit activity of locus coeruleus neurons in the freely moving cat. I. During naturalistic behaviors and in response to simple and complex stimuli. *Brain Res.* **371**, 324–334 (1986).
- Foote, S. L., Aston-Jones, G. & Bloom, F. E. Impulse activity of locus coeruleus neurons in awake rats and monkeys is a function of sensory stimulation and arousal. *Proc. Natl Acad. Sci. USA* **77**, 3033–3037 (1980).
- Shouse, M. N., Staba, R. J., Saquib, S. F. & Farber, P. R. Monoamines and sleep: microdialysis findings in pons and amygdala. *Brain Res.* **860**, 181–189 (2000).
- Léna, I. et al. Variations in extracellular levels of dopamine, noradrenaline, glutamate, and aspartate across the sleep–wake cycle in the medial prefrontal cortex and nucleus accumbens of freely moving rats. *J. Neurosci. Res.* **81**, 891–899 (2005).
- Yamaguchi, H., Hopf, F. W., Li, S.-B. & Lecea, L. In vivo cell type-specific CRISPR knockdown of dopamine beta hydroxylase reduces locus coeruleus evoked wakefulness. *Nat. Commun.* **9**, 5211 (2018).
- Rajkowski, J., Kubiak, P. & Aston-Jones, G. Locus coeruleus activity in monkey: phasic and tonic changes are associated with altered vigilance. *Brain Res. Bull.* **35**, 607–616 (1994).
- Swift, K. M. et al. Abnormal locus coeruleus sleep activity alters sleep signatures of memory consolidation and impairs place cell stability and spatial memory. *Curr. Biol.* **28**, 3599–3609 (2018).
- Lecci, S. et al. Coordinated infraslow neural and cardiac oscillations mark fragility and offline periods in mammalian sleep. *Sci. Adv.* **3**, e1602026 (2017).
- Osorio-Forero, A. et al. Noradrenergic circuit control of non-REM sleep substates. *Curr. Biol.* **31**, 5009–5023 (2021).
- Novitskaya, Y., Sara, S. J., Logothetis, N. K. & Eschenko, O. Ripple-triggered stimulation of the locus coeruleus during post-learning sleep disrupts ripple/spindle coupling and impairs memory consolidation. *Learn. Mem.* **23**, 238–248 (2016).
- Feng, J. et al. A genetically encoded fluorescent sensor for rapid and specific in vivo detection of norepinephrine. *Neuron* **102**, 745–761 (2019).
- Osorio-Forero, A. et al. Infraslow locus coeruleus activity coordinates spindle rhythms and heart rate to gate fluctuating non-REM sleep substates. Preprint at <https://www.biorxiv.org/content/10.1101/2021.03.08.434399v1> (2021).
- EEG arousals: scoring rules and examples: a preliminary report from the sleep disorders atlas task force of the American sleep disorders association. *Sleep* **15**, 173–184 (1992).
- Gottesmann, C. The transition from slow-wave sleep to paradoxical sleep: evolving facts and concepts of the neurophysiological processes underlying the intermediate stage of sleep. *Neurosci. Biobehav. Rev.* **20**, 367–387 (1996).
- Krueger, J. N. et al. Amnesia for context fear is caused by widespread disruption of hippocampal activity. *Neurobiol. Learn. Mem.* **175**, 107295 (2020).
- Takeuchi, T. et al. Locus coeruleus and dopaminergic consolidation of everyday memory. *Nature* **537**, 357–362 (2016).
- Mahn, M., Prigge, M., Ron, S., Levy, R. & Yizhar, O. Biophysical constraints of optogenetic inhibition at presynaptic terminals. *Nat. Neurosci.* **19**, 554 (2016).
- de Medeiros, M. A., Reis, L. C. & Mello, L. E. Stress-induced c-Fos expression is differentially modulated by dexamethasone, diazepam and imipramine. *Neuropsychopharmacology* **30**, 1246–1256 (2005).
- Mayers, A. G. & Baldwin, D. S. Antidepressants and their effect on sleep. *Hum. Psychopharmacol.* **20**, 533–559 (2005).
- Mitchell, H. A. & Weinshenker, D. Good night and good luck: norepinephrine in sleep pharmacology. *Biochem. Pharmacol.* **79**, 801–809 (2010).
- Watts, A., Gritton, H. J., Sweigart, J. & Poe, G. R. Antidepressant suppression of non-REM sleep spindles and REM sleep impairs hippocampus-dependent learning while augmenting striatum-dependent learning. *J. Neurosci.* **32**, 13411–13420 (2012).
- Porter-Stransky, K. A. et al. Noradrenergic transmission at alpha-1 adrenergic receptors in the ventral periaqueductal gray modulates arousal. *Biol. Psychiatry* **85**, 237–247 (2019).
- Rudzik, F. et al. Sleep spindle characteristics and arousability from nighttime transportation noise exposure in healthy young and older individuals. *Sleep* **41**, zsy077 (2018).
- Peter-Derex, L., Yammine, P., Bastuji, H. & Croisile, B. Sleep and Alzheimer's disease. *Sleep. Med. Rev.* **19**, 29–38 (2015).
- Scammell, T. E., Arrigoni, E. & Lipton, J. O. Neural circuitry of wakefulness and sleep. *Neuron* **93**, 747 (2017).
- Luppi, P. H., Aston-Jones, G., Akaoka, H., Chouvet, G. & Jouvet, M. Afferent projections to the rat locus coeruleus demonstrated by retrograde and anterograde tracing with cholera-toxin B subunit and Phaseolus vulgaris leucoagglutinin. *Neuroscience* **65**, 119–160 (1995).
- Aston-Jones, G., Ennis, M., Pieribone, V. A., Nickell, W. T. & Shipley, M. T. The brain nucleus locus coeruleus: restricted afferent control of a broad efferent network. *Science* **234**, 734–737 (1986).
- Picchioni, D. et al. Autonomic arousals contribute to brain fluid pulsations during sleep. *Neuroimage* **249**, 118888 (2022).
- Fultz, N. E. et al. Coupled electrophysiological, hemodynamic, and cerebrospinal fluid oscillations in human sleep. *Science* **366**, 628–631 (2019).
- Purcell, S. M. et al. Characterizing sleep spindles in 11,630 individuals from the National Sleep Research Resource. *Nat. Commun.* **8**, 15930 (2017).
- Dringenberg, H. C. & Olmstead, M. C. Integrated contributions of basal forebrain and thalamus to neocortical activation elicited by pedunculopontine tegmental stimulation in urethane-anesthetized rats. *Neuroscience* **119**, 839–853 (2003).

47. Gervasoni, D. et al. Effect of chronic treatment with milnacipran on sleep architecture in rats compared with paroxetine and imipramine. *Pharmacol. Biochem. Behav.* **73**, 557–563 (2002).
48. Jones, B. E. The role of noradrenergic locus coeruleus neurons and neighboring cholinergic neurons of the pontomesencephalic tegmentum in sleep–wake states. *Prog. Brain Res.* **88**, 533–543 (1991).
49. Williams, J. A. & Reiner, P. B. Noradrenaline hyperpolarizes identified rat mesopontine cholinergic neurons in vitro. *J. Neurosci.* **13**, 3878–3883 (1993).
50. Latchoumane, C.-F. V., Ngo, H.-V. V., Born, J. & Shin, H.-S. Thalamic spindles promote memory formation during sleep through triple phase-locking of cortical, thalamic, and hippocampal rhythms. *Neuron* **95**, 424–435 (2017).
51. Li, W., Ma, L., Yang, G. & Gan, W.-B. REM sleep selectively prunes and maintains new synapses in development and learning. *Nat. Neurosci.* **20**, 427–437 (2017).
52. Ribeiro, S. et al. Novel experience induces persistent sleep-dependent plasticity in the cortex but not in the hippocampus. *Front. Neurosci.* **1**, 43–55 (2007).
53. Giuditta, A. et al. The sequential hypothesis of the function of sleep. *Behav. Brain Res.* **69**, 157–166 (1995).
54. Gais, S., Rasch, B., Dahmen, J. C., Sara, S. & Born, J. The memory function of noradrenergic activity in non-REM sleep. *J. Cogn. Neurosci.* **23**, 2582–2592 (2011).
55. Rasch, B., Pommer, J., Diekelmann, S. & Born, J. Pharmacological REM sleep suppression paradoxically improves rather than impairs skill memory. *Nat. Neurosci.* **12**, 396–397 (2008).
56. Aghajanian, G. K. & VanderMaelen, C. P.  $\alpha_2$ -adrenoceptor-mediated hyperpolarization of locus coeruleus neurons: intracellular studies in vivo. *Science* **215**, 1394–1396 (1982).
57. Washburn, M. & Moises, H. C. Electrophysiological correlates of presynaptic alpha 2-receptor-mediated inhibition of norepinephrine release at locus coeruleus synapses in dentate gyrus. *J. Neurosci.* **9**, 2131–2140 (1989).
58. Hayat, H. et al. Locus coeruleus norepinephrine activity mediates sensory-evoked awakenings from sleep. *Sci. Adv.* **6**, eaaz4232 (2020).
59. Oe, Y. et al. Distinct temporal integration of noradrenaline signaling by astrocytic second messengers during vigilance. *Nat. Commun.* **11**, 471 (2020).

**Publisher's note** Springer Nature remains neutral with regard to jurisdictional claims in published maps and institutional affiliations.

© The Author(s), under exclusive licence to Springer Nature America, Inc. 2022



## Methods

**Mice.** Wild-type C57BL/6 mice were acquired from Janvier Labs at 7 weeks of age. Heterozygous TH::Cre mice were bred on a C57BL/6 background. Both male and female mice were used. Animals were housed with unlimited access to food and water on a normal 12-hour light/dark cycle at 21 °C with 40–60% humidity. Animals were 12–20 weeks old at the time of behavioral assessment. All experiments were approved by the Danish Animal Experiments Inspectorate and were overseen by the University of Copenhagen Institutional Animal Care and Use Committee, in compliance with the European Communities Council Directive of 22 September 2010 (2010/63/EU) legislation governing the protection of animals used for scientific purposes.

**Surgery.** All surgeries were performed in accordance with institutional guidelines. Mice were 7–15 weeks old at the time of surgery. General anesthesia was induced using 5% isoflurane and maintained at 1–3% isoflurane. The mice were placed in a stereotaxic frame and received pre-operative buprenorphine (0.05 mg kg<sup>-1</sup>) for general analgesia along with lidocaine (0.03 mg kg<sup>-1</sup>) at the incision site. An incision was made on the scalp between the ears, and the skull was aligned. Four burr holes were drilled in the skull with an electrical drill (Tech 2000, RAM Microtorque) according to stereotaxic coordinates relative to bregma. In mPFC, we injected AAV9-hSyn-GRAB<sub>NE2m</sub> under the neuronal hSyn promoter (provided by Yulong Li). Simultaneously, we injected AAV5 encoding floxed GCaMP6f in LC in a TH-Cre driver mouse line. Stereotaxic coordinates used for mPFC injections: A/P +1.7 mm, M/L -0.3 mm and D/V -2.00 mm, -2.25 mm, -2.50 mm and -2.75 mm (125 nl of virus infused at each depth); and for LC injections: A/P -5.5 mm, M/L -0.9 mm and D/V -3.2 mm, -3.4 mm, -3.6 mm and -3.8 mm (125 nl at each depth). Virus was infused at 100 nl min<sup>-1</sup>, and the needle was left in place for an additional 7 minutes and then slowly withdrawn. Then, 0.8-mm low-impedance stainless steel screws (NeuroTek) were screwed into two burr holes located above frontal cortex (contralateral side from the optic implant) and above the cerebellum (reference area). Two silver wires (W3 Wire International) were inserted into the trapezius muscle serving as an EMG electrode. Mono fiberoptic cannulas (400 μm, 0.48 NA, Doric Lenses) attached to a 2.5-mm-diameter metal ferrule were then implanted in mPFC (A/P 1.7 mm, M/L -0.3 mm, D/V -2.50 mm) and LC (A/P -5.5 mm, M/L -0.9 mm, D/V -3.65 mm), and cannulas and screws were fixed to the skull using dental cement (SuperBond). Before waking up, animals received carprofen (5 mg kg<sup>-1</sup>) subcutaneously. A minimum of 2 weeks were allowed for sufficient expression and recovery.

For optogenetic LC experiments, AAV5/2 encoding floxed ArchT-eGFP or floxed hChR2-eYFP were injected bilaterally in LC at A/P -5.5 mm, M/L ±0.9 mm and D/V -3.75 mm (300 nl of virus), and dual fiberoptic cannula (200 μm, 0.22 NA, Doric Lenses) were implanted above LC (D/V -3.65 mm).

Construct	Company/provider	Cat. no.
pAAV9-hSyn-GRAB <sub>NE2m</sub>	Yulong Li Lab	
AAV5-Syn-FLEX-GCaMP6 f-WPRE-SV40	Addgene	100833-AAV5
pAAV-hSyn-GRAB <sub>NEmut</sub>	Addgene	123310-AAVg
ssAAV5/2-shortCAG-dlox-ArchT-eGFP-dlox-WPRE-SV40p(A)	Zürich Vector Core	V461-5
ssAAV5/2-hEF1a-dlox-hChR2(H134R)-eYFP(rev)-dlox-WPRE-hGHp(A)	Zürich Vector Core	v214-5
AAV5-EF1a-DIO-EYFP	UNC Vector Core	
pAAV9-hSyn-GRAB <sub>DAlh</sub>	Addgene	113050-AAV9

**Fiber photometry.** Two pairs of excitation LEDs (465 nm and 405 nm, Doric Lenses, Tucker-Davis Technologies) were connected to each minicube (Doric Lenses) by attenuator patch cords (400-μm core, NA 0.48, Doric Lenses). The minicube optics allow for monitoring of fluorophores using dichroic mirrors and cleanup filters chosen to match the excitation and emission spectra. LEDs were controlled by LED drivers (Thorlabs, Doric Lenses, Tucker-Davis Technologies) and connected to an RZ-5 or RZ10-X real-time processor (Tucker-Davis Technologies). In mPFC, 465-nm and 405-nm excitation light was delivered through the same patch cord to excite GRAB<sub>NE2m</sub> fluorescence, whereas 405-nm was an excitation isosbestic wavelength for GCaMP6f correcting for bleaching and signal fluctuations due to movement. In LC, using the same patch cord, excitation light at 465 nm was used to stimulate GCaMP6f fluorescence, and 405 nm was added as control. Then, 465-nm/405-nm excitation was sinusoidally modulated at 531 Hz/211 Hz. Fiberoptic patch cords (400-μm core, NA 0.48, Doric Lenses) provided a light path between the minicubes and the animals. Zirconia sleeves were used to attach fiberoptic patch cords to fiber implants on the animal.

Each of the four modulated signals generated by the four LEDs were independently recovered using standard synchronous demodulation techniques implemented on the RZ-5/RZ10-X real-time processor (sampling rate of 1,000 Hz). Synapse software (Tucker-Davis Technologies) was used to control the signal

processor and align fluorescent signals with video and EEG/EMG signals through in-coming or out-coming TTL pulses. Files were exported for analysis to MATLAB R2020a (MathWorks).  $\Delta F/F$  calculations were based on the fitted 405-nm signal or by using the median of the fluorescence signal itself. For 405 fitting, first, the scale of the 465-nm signal and isosbestic 405 channel was normalized by using a least squares (MATLAB polyfit function) to determine the slope and intercept needed to generate a scaled 405-nm channel:

$$\text{scaled 405 nm channel} = a * 405 \text{ nm channel} + b$$

Next,  $\Delta F/F$  is generated by subtracting the fitted control channel from the signal channel:

$$\Delta F/F (\%) = (\text{signal 465 nm} - \text{scaled 405 channel}) * 100 / \text{scaled 405 channel}$$

To characterize NE oscillations across all NREM and REM sleep phases, we calculated NE peak level (90% percentile) and NE trough level (10% percentile) across NREM or REM sleep phases, respectively, during 3 hours of sleep recordings. NE amplitude was calculated by subtracting NE trough values from NE peak values. The oscillation frequency of NE was calculated by selecting NE peaks throughout NREM sleep across 3 hours of sleep recordings (MATLAB findpeaks function, minimum inter-trial interval of 10 seconds, minimum amplitude of 1.5  $\Delta F/F$  (%)) and dividing it by the total duration of NREM sleep. Multi-taper power spectral analysis was done on NE traces across NREM sleep, REM sleep and wake to assess low-frequency oscillatory patterns (MATLAB pmtm function).

To characterize NE signal across MA<sup>NE</sup>, MA<sup>EEG/EMG</sup> and wake<sup>EEG/EMG</sup> transitions, NE signal was aligned according to the minimum NE trough level immediately preceding the transition, and summarized NE trough levels were calculated by taking the 10% percentile from -10 seconds to 0 seconds and NE peak level (90th percentile) from 0 seconds to 50 seconds. The NE ascend amplitude was defined as the difference between NE peak and trough. NE descend time and slope was calculated by finding the onset of maximal NE peak preceding the descend and calculating the distance between this point and the minimal NE trough value. Slope of the NE signal between these values was calculated by a linear regression fit. With optogenetic suppression of LC, the NE descend amplitude induced by laser onset was calculated by subtracting the 5% percentile from 90 seconds after onset from the mean value 60 seconds before onset, whereas the NE ascent amplitude at laser offset was calculated by subtracting 95% percentile 90 seconds after offset from the mean value 60 seconds before offset.

**Sleep measurements.** Mice were placed in recording chambers (ViewPoint Behavior Technology), and cables were connected to the EEG and EMG electrodes. Cables were connected to a commutator (Plastics One, Bilaney, SL12C), and the mice were allowed to habituate to the recording chamber (ViewPoint Behavior Technology) for at least 1 day before recordings. On the day of recording, mice were connected to fiberoptic implants, and recordings were done for 2–4 hours during their light phase. EEG and EMG signals were amplified (National Instruments, 16-channel AC amplifier, model 3500) and filtered (EEG signal: high-pass at 1 Hz and low-pass at 100 Hz; EMG signal: high-pass at 10 Hz and low-pass at 100 Hz), and a notch filter of 50 Hz was used to reduce power line noise. Signals were digitized using a Multifunction I/O DAQ device (National Instruments, USB-6343) and sampled at a sampling rate of 512 Hz. Video was recorded continuously using an infrared camera (FLIR Systems) and used later to aid in the scoring of vigilance states. Hypnograms were created by visual inspection of EEG traces divided into 5-second and, subsequently, 1-second epochs. Vigilance states were defined as wake (high muscle tonus and a high-frequency, low-amplitude EEG), NREM sleep (no muscle tonus and low-frequency, high-amplitude EEG) and REM sleep (no muscle tonus and high-frequency, low-amplitude EEG). We categorized wake bouts of <15 seconds as micro-arousals (Fig. 1b). In addition, we defined local EEG changes (combined theta, sigma and beta power reductions; Extended Data Fig. 1) without EMG changes during NREM sleep as MA<sup>NE</sup>. Analysis of hypnograms was done using SleepScore software (ViewPoint Behavior Technology). All data analysis was subsequently performed in MATLAB using custom-made scripts. The power spectral densities at frequencies 1–30 Hz were calculated using Welch's method with a 5-second Hamming window, and the logarithm of the power was calculated for each frequency. The average power for different frequency bands was determined (delta: 1–4; theta: 4–8; sigma: 8–15; beta: 15–30). To detect spindles, collected LFP signal in the S1 cortex ( $n=4$ ) was bandpass filtered in the 8–15 frequency range and subsequently squared. A threshold of 0.8 times the standard deviation above the mean value was applied to the smoothed trace, and peaks crossing this threshold and lasting >0.5–10 seconds were marked as putative spindles. Events separated by <20 ms were merged as a single event. In all sleep recordings without interventions (Figs. 1 and 2), two mice were excluded from subpanels relating to LC Ca<sup>2+</sup> measurements due to mistargeting of virus injection, and one mouse was excluded from REM sleep analysis due to no REM sleep episodes >150 s.

Cross-correlation analysis between continuous recordings of NE levels and sigma or delta power traces was done across 10-minute NREM sleep periods. Specifically, NE recordings were downsampled 100 times, and corresponding sigma or delta power calculations were upsampled to match the NE recordings.

In a subset of sleep recordings, animals ( $n=7$ ) were administered desipramine ( $10\text{ mg kg}^{-1}$ ,  $10\text{ ml kg}^{-1}$ ) by intraperitoneal injection and left to record for 3.5 hours. On another day (minimum 3 days apart from the desipramine injection), the same animals underwent similar recordings where they received a saline injection ( $10\text{ ml kg}^{-1}$ ) to get within-animal controls. Analysis was done on a 1–3.5-hour period after administration due to difficulties classifying sleep based on EEG patterns during the first hour after administration.

**Auditory stimulation.** During sleep recordings as described above, a new batch of mice ( $n=6$ ) was subjected to auditory stimulations (0.5 seconds, 80 dB) at a 4-minute interval. Subsequently, sounds during NREM sleep were selected and divided into outcome (sleep/arousal) based on the reduction in the sigma power ( $> 0.1\text{ log}(\mu\text{V}^2)$ ) within 5 seconds after the sound.

**Optogenetic inhibition of LC.** A 532-nm laser (Changchun New Industries Optoelectronics Technology Co. Ltd., model 16030476) was used to generate 2-minute stimulations (2.5 mW at the tip of each fiber) bilaterally in LC simultaneously with mPFC fiber photometry recordings and EEG and EMG measurements. Mice were left undisturbed in EEG recording chambers during the light phase, allowing for natural sleep–wake behavior, while being recorded on infrared camera. Animals were stimulated every 10 minutes regardless of vigilance state. Stimulations initiated during NREM sleep were subsequently selected for analysis.  $n=9$  Arch and  $n=5$  YFP; however, one Arch mouse was excluded from subpanels relating to NE measurements due to low GRAB<sub>NE2m</sub> expression ( $n=8$ ), and one YFP mouse was excluded from subpanels relating to sigma power due to noisy EEG signal ( $n=4$ ).

**Optogenetic activation of LC.** A 430–490-nm laser (Shanghai Laser & Optics Century Co. Ltd., model BL473–200FC) was used to generate 2-second stimulations of 10-ms pulses at 20 Hz (5 mW at each fiber tip) bilaterally in LC simultaneously with GRAB<sub>NE2m</sub> recordings from mPFC. Two hours of baseline recordings without laser stimulation was followed by 5 hours of closed-loop stimulation where threshold crossing of smoothed real-time calculation of  $\Delta F/F$  (%) calculations of NE levels based on 2-minute windows (Synapse, Tucker-Davis Technologies) elicited laser stimulations. Thresholds were set at  $-15\ \Delta F/F$  (%) and increased in increments of  $5\ \Delta F/F$  (%) once per hour until  $+5\ \Delta F/F$  (%). After the 5 hours of laser stimulations, recording continued for another 2 hours without laser stimulations. All output measurements from laser manipulation (Fig. 4d,f–j) are normalized within animal to the baseline value before the first laser stimulation period.  $n=7$  Chr2 and  $n=7$  YFP; however, one YFP mouse was excluded in subpanels relating to sigma power due to noisy EEG signal ( $n=6$ ).

**Novel object recognition.** Animals were habituated to an open field for 10 minutes, followed by a resting period in their home cage for 5 minutes while two identical objects were placed in the open field. The animals were then habituated to the objects for 15 minutes, followed by desipramine administration ( $10\text{ mg kg}^{-1}$ ,  $10\text{ ml kg}^{-1}$ ,  $n=7$ ) or saline ( $10\text{ ml kg}^{-1}$ ,  $n=9$ ) and allowed to sleep for 3 hours. A novel object replaced one of the familiar objects, and the animals were allowed to explore the two objects for 5 minutes. A separate group of animals expressing Arch ( $n=9$ ) in LC for optogenetic suppression or YFP ( $n=5$ ) were habituated to initial objects for 10 minutes, followed by 2 hours in the EEG recording chamber, where we recorded EEG, EMG and GRAB<sub>NE2m</sub> fluorescence while the animals were optogenetically stimulated as described above but with 2-minute stimulations every 6 minutes before 5 minutes of novel object exposure. In another group of animals expressing either Chr2 ( $n=7$ ) or YFP ( $n=7$ ) in LC for optogenetic activation, animals were familiarized with two objects for 15 minutes to ensure that YFP control could remember the objects. Animals were then allowed to sleep for 2 hours while being optogenetically stimulated with a GRAB<sub>NE2m</sub> threshold = 0 as described above before 5 minutes of novel object exposure. This was all done during the light phase to encourage natural sleep between the encoding and recall phase. EthoVision XT 11.5 (Noldus) was used to track videos of the behavioral tasks.

**Immunohistochemistry.** To validate location of optic implant and virus expression, we did immunostaining on brain sections. Animals were deeply anesthetized using ketamine–xylazine and then perfused with PBS followed by 4% paraformaldehyde (PFA). Brains were dissected and post-fixed in 4% PFA overnight and transferred to PBS until sectioning. Next, 60- $\mu\text{m}$  sections surrounding the implants were cut using a vibratome. Sections were then blocked in PBS with 5% goat serum and 0.3% Triton X-100 at room temperature for 1–2 hours before overnight incubation with primary antibodies at 4°C. After washing, sections were incubated with secondary antibodies at room temperature for 2 hours and then incubated with DAPI for 2–10 minutes.

Images of whole brain slices were acquired using a Nikon Instruments Ni-E motorized microscope equipped with a  $\times 4$  CFI Plan Apo Lambda objective (0.2 NA). For excitation, a halogen light source was used in combination with excitation filters 362–389 nm, 465–495 nm, 530–575 nm and Cy5 628–640 nm.  $4 \times 4$  images were acquired per section and stitched together automatically using NIS Elements AR software from Nikon. Closeup images were acquired using a Nikon Instruments C2+ Ti-E confocal laser scanning microscope with a  $\times 20$  CFI Plan Fluor MI objective (0.75 NA) or a  $\times 40$  CFI Plan Fluor oil objective (1.30 NA).

The excitation sources were 405-nm, 561-nm and 640-nm laser diodes and a 488-nm solid-state diode laser. For the  $\times 40$  images, we acquired Z-stacks ranging from 20  $\mu\text{m}$  to 40  $\mu\text{m}$  and flattened them in Fiji/ImageJ using standard deviation of intensity.

#### Primary antibodies.

Name	Company/provider	Cat. no.
Anti-RFP antibody, 1:500	Abcam	ab62341
Anti-GFP (green fluorescent protein) (chicken antibodies, IgY fraction), 1:500	Aves	GFP-1020
GFP polyclonal antibody, 1:500	Thermo Fisher Scientific	A-6455
Mouse anti-neuronal nuclei (NeuN) monoclonal antibody, clone A60, 1:100	Merck Millipore	MAB377
Anti-tyrosine hydroxylase, clone LNC1, 1:500	Merck Millipore	MAB318

#### Secondary antibodies.

Name	Company/provider	Cat. no.
Goat anti-rabbit IgG (H+L) highly cross-adsorbed secondary antibody, Alexa Fluor 488	Thermo Fisher Scientific	A11034
Goat anti-chicken IgY (H+L) secondary antibody, Alexa Fluor 488	Thermo Fisher Scientific	A11039
Goat anti-rabbit IgG (H+L) cross-adsorbed secondary antibody, Alexa Fluor 568	Thermo Fisher Scientific	A11011
Goat anti-chicken IgY (H+L) secondary antibody, Alexa Fluor 568	Thermo Fisher Scientific	A11041
Goat anti-mouse IgG1 cross-adsorbed secondary antibody, Alexa Fluor 647	Thermo Fisher Scientific	A21240

**High-performance liquid chromatography.** Tissue samples ( $n=11$ ) were immediately frozen on dry ice and stored at  $-80^\circ\text{C}$  until homogenized in 250  $\mu\text{l}$  of perchloric acid 0.1 N. After centrifugation at 14,000g for 30 minutes, 200  $\mu\text{l}$  of the supernatant was filtered through a glass 0.22- $\mu\text{m}$  filter (Avantec, 13CP020AS). The samples were analyzed using high-performance liquid chromatography (HPLC) with electrochemical detection methodology. The concentrations of monoamines and metabolites were determined by HPLC with electrochemical detection. The column was a Prodigy 3- $\mu\text{m}$  ODS-3 C18 (DA  $2 \times 100\text{ mm}$ , particle size 3  $\mu\text{m}$ , Phenomenex, YMC Europe). The mobile phase (55 mM sodium acetate, 1 mM octanesulfonic acid, 0.1 mM Na<sub>2</sub>EDTA and 8% acetonitrile, pH 3.2) was de-gassed with an online de-gasser. Samples (10  $\mu\text{l}$ ) were injected with a flow rate of 0.15 ml min<sup>-1</sup>. Electrochemical detection was accomplished using an amperometric detector (Antec DECADE) with a glassy carbon electrode set at 0.8 V and an Ag/AgCl reference electrode. The output was recorded, and peak areas were calculated by LC solution software (Shimadzu).

**Foot shock with GRAB<sub>DA1h</sub> sensor.** Fiber photometry measurements were obtained from mice ( $n=5$ ) expressing the dopamine sensor GRAB<sub>DA1h</sub> in mPFC (surgery as described above) during a foot shock paradigm with pharmacological blocking of dopamine re-uptake. The mice were habituated to a foot shock chamber for 5 minutes before receiving foot shocks (0.45 mA, 0.5 seconds) every 3 minutes until a total of 11 foot shocks. After the third foot shock, mice received a dose of GBR 12909 hydrochloride (Tocris, cat. no. 0421) via an intraperitoneal injection ( $10\text{ mg kg}^{-1}$ ,  $10\text{ ml kg}^{-1}$ ) or saline ( $10\text{ ml kg}^{-1}$ ).

**Statistics and reproducibility.** No statistical methods were used to pre-determine sample sizes, but our sample sizes are similar to those reported in previous publications<sup>15,22</sup>. Manipulations were counterbalanced and randomized across mice. Most data collection and analysis were not performed blinded to the conditions owing to the automatic nature of the experiments and analysis. The Shapiro–Wilk test was used to assess normality of data. Two-sided paired *t*-test or unpaired *t*-test was employed to compare pairs of groups, if data passed the normality test. Otherwise, the Wilcoxon matched-pairs signed-rank test or Mann–Whitney test was used for comparison. One-sample *t*-test was used to test whether population mean was different from a specific value. For repeated measurements, one-way or two-way ANOVAs with Sidak's post hoc test were used, respectively.

Immunohistochemical experiments were repeated independently with similar results in up to three animals.

**Reporting summary.** Further information on research design is available in the Nature Research Reporting Summary linked to this article.

### Data availability

The datasets generated during and/or analyzed in this study are available from the corresponding author upon reasonable request. Source data are provided with this paper.

### Code availability

The custom-made MATLAB code used in this study is available from GitHub: <https://github.com/MieAndersen/NE-oscillations>.

### Acknowledgements

Funding: Lundbeck Foundation, R386–2021–165; Independent Research Council Denmark, 7016–00324A; Augustinus Foundation, 16–3735; Novo Nordisk Foundation, NNF20OC0066419; US Department of Health & Human Services, National Institutes of Health (NIH), R01AT011439; US Department of Defense, Army Research Office, W911NF1910280; The Simons Foundation, 811237; Adelson Foundation; National Key R&D Program of China, 2021YFF0502904; National Natural Science Foundation of China, 31925017 and 31871087; NIH BRAIN Initiative, 1U01NS113358 and 1U01NS120824; and the FENG Foundation. We thank Myles Billard for technical support and Dan Xue for graphical assistance.

### Author contributions

Conceptualization: C.K., M.A., H.H., M.N. and P.W. Fiber photometry and EEG methodology and investigation: C.K., M.A., N.H., C.D. and V.U. Viral constructs: Y.L., J.F. and F.D. HPLC methodology: P.W. Analysis: C.K., M.A. and B.S. Visualization: C.K. and M.A. Supervision: H.H. and M.N. Writing—original draft: C.K. and M.A. Writing—review and editing: C.K., M.A., H.H. and M.N.

### Competing interests

The authors declare no competing interests.

### Additional information

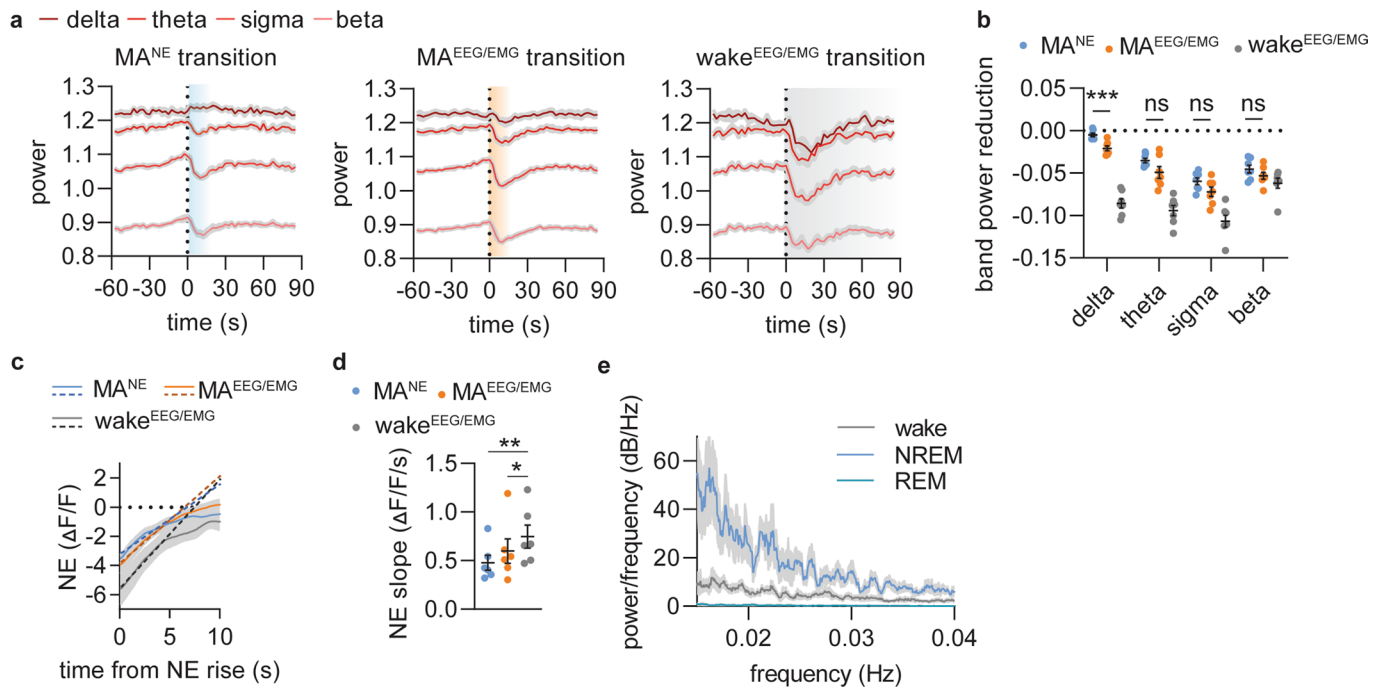
**Extended data** is available for this paper at <https://doi.org/10.1038/s41593-022-01102-9>.

**Supplementary information** The online version contains supplementary material available at <https://doi.org/10.1038/s41593-022-01102-9>.

**Correspondence and requests for materials** should be addressed to Celia Kjaerby or Maiken Nedergaard.

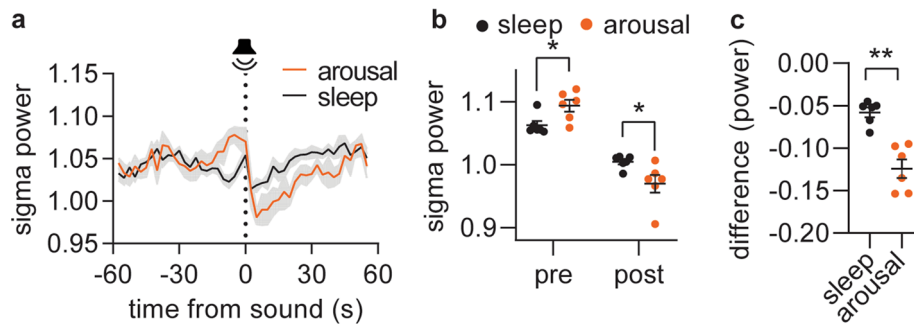
**Peer review information** *Nature Neuroscience* thanks the anonymous reviewers for their contribution to the peer review of this work.

**Reprints and permissions information** is available at [www.nature.com/reprints](http://www.nature.com/reprints).

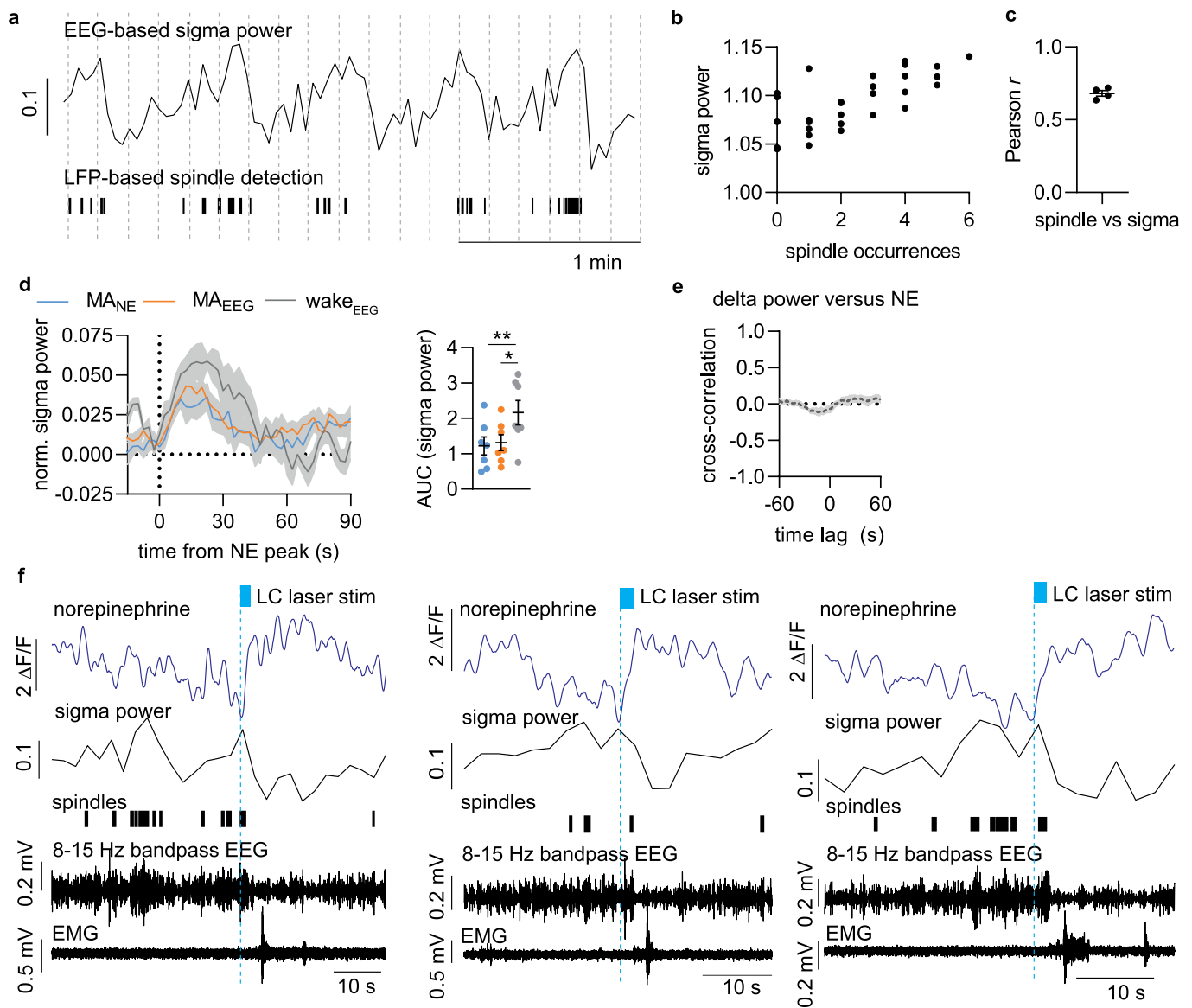


**Extended Data Fig. 1 | All ascending stages of NE oscillations are associated with EEG-defined micro-arousals or awakenings.** **a**, Mean power traces for delta, theta, sigma and beta frequency bands aligned to NE rise associated with EEG/EMG-based transitions from NREM sleep to continued NREM sleep (blue, MA<sup>NE</sup>), micro-arousals (MA<sup>EEG/EMG</sup>, orange) and wake (grey, wake<sup>EEG/EMG</sup>). **b**, Summary plot showing the reduction in band power across the different transitions. There was no difference between MA<sup>NE</sup> and MA<sup>EEG/EMG</sup> for theta, sigma and beta band power, which are the frequencies used to assess micro-arousals. Significance was calculated by means of two-way repeated measures ANOVA with Šídák's post hoc test (only MA<sup>NE</sup> and MA<sup>EEG/EMG</sup> post hoc comparisons shown in graph for simplicity,  $P=0.0003$ , delta;  $P=0.13$ , theta;  $P=0.11$ , sigma;  $P=0.65$ , beta). **c**, Slope of linear regression on 5 initial seconds of NE rise was used as estimate for rise time. **d**, NE slope across the different type of transitions (repeated measures one-way ANOVA with Tukey's multiple comparisons test,  $P=0.0059$ , MA<sup>NE</sup> vs wake;  $P=0.041$ , MA<sup>EEG/EMG</sup> vs wake). **e**, Multi-taper power spectral analysis showed increased power for slower frequencies for NREM sleep compared to wake and REM sleep with no defined peak frequency likely due to the discrete nature of NE oscillations.  $n=7$ . Data is shown as mean  $\pm$  SEM. \* $P < 0.05$ , \*\* $P < 0.01$ , \*\*\* $P < 0.001$ .

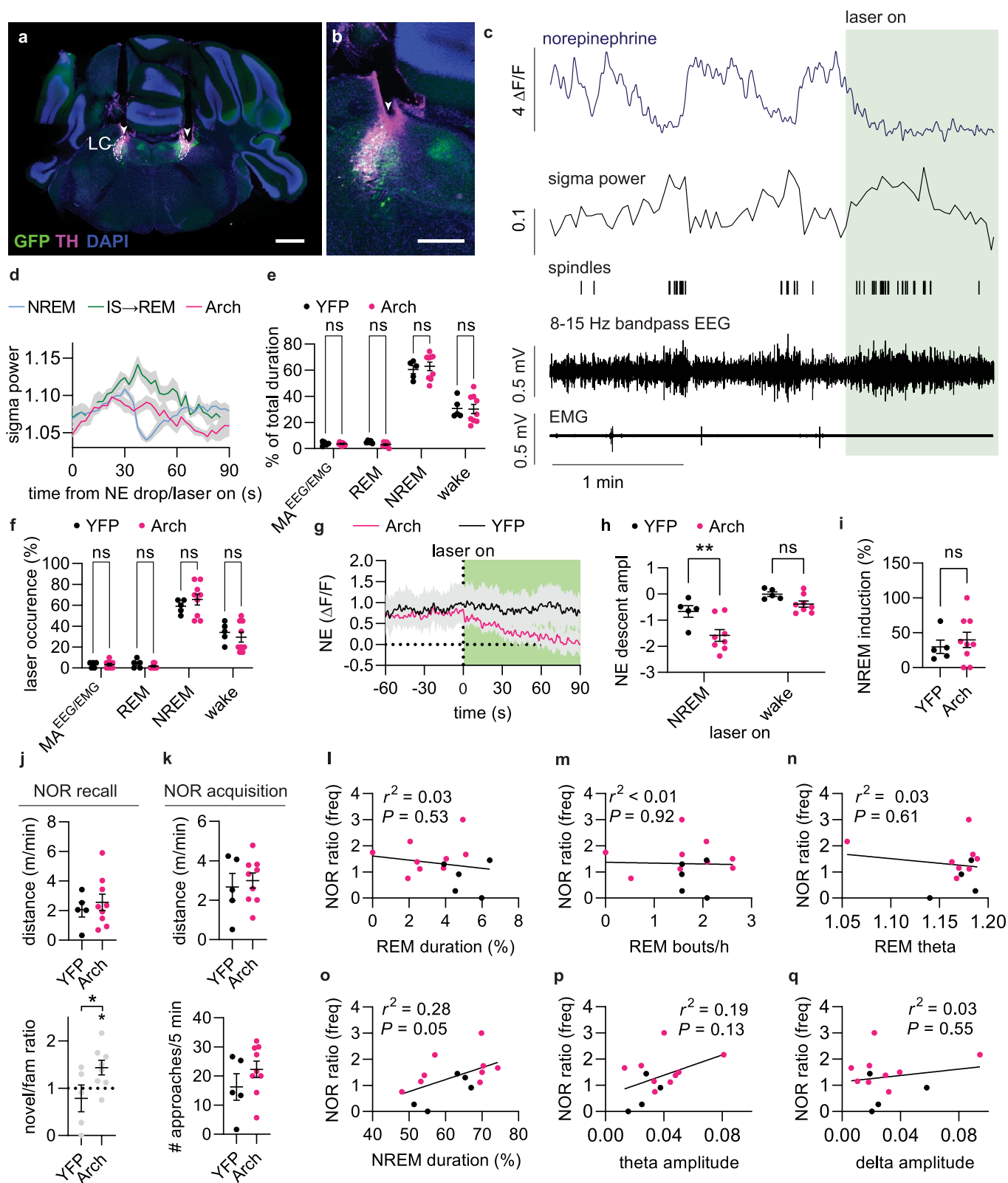




**Extended Data Fig. 2 | Decrease in sigma power marks tone-evoked arousal.** Based on the local decline in sigma power in response to tone ( $> 0.1 \log(\mu V^2)$ ), the tone outcome was divided into arousal and otherwise maintained sleep. **a**, Mean sigma power traces in response to tone leading to either arousal or persistent sleep. **b**, The maximum value of sigma power maximum prior to tone ('pre') and the minimum sigma power after the tone ('post') for the defined arousal and sleep conditions. **c**, The difference in sigma power occurring in response to the tone. Significance was calculated by means of two-way repeated measures ANOVA with Šídák's post hoc test (**b**,  $P=0.035$ , pre;  $P=0.023$ , post) or two-tailed paired  $t$ -test (**c**,  $P=0.0034$ ).  $n=6$ . Data is shown as mean  $\pm$  SEM. \* $P < 0.05$ , \*\* $P < 0.01$ .



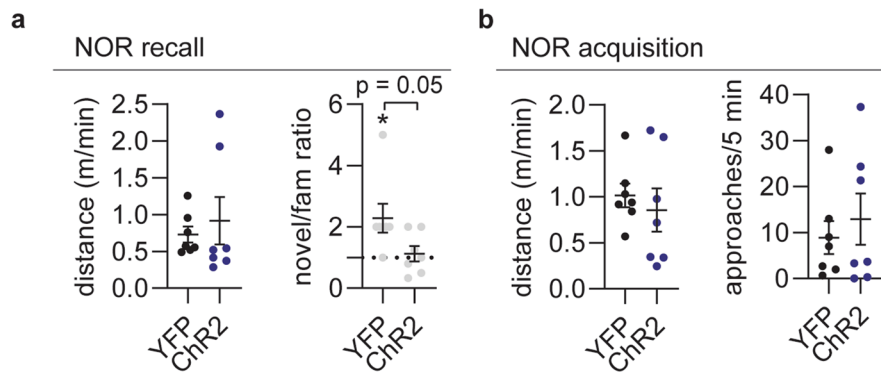
**Extended Data Fig. 3 | Relationship between norepinephrine, sigma power, spindles and delta power.** **a**, Representative trace showing sigma power of surface EEG recordings with corresponding detection of spindles based on S1 cortical LFP recordings. **b**, Correlation between spindle occurrences and mean sigma power across 10 s bins over a 5 min NREM sleep episode. **c**, Mean Pearson  $r$  values ( $0.63 \pm 0.02$ ). **d**, Mean sigma power traces normalized to baseline showing the amount of sigma power increase associated with NE descents preceding microarousals ( $MA_{NE}$  or  $MA_{EEG/EMG}$ ) or awakenings ( $wake_{EEG/EMG}$ ). Calculated area under the curve (AUC) for sigma power is largest during the NE descents associated with awakenings transitions (two-tailed paired  $t$ -test;  $P=0.60$ ,  $MA_{NE}$  vs  $MA_{EEG/EMG}$ ;  $P=0.0057$ ,  $MA_{NE}$  vs wake;  $P=0.044$ ,  $MA_{EEG/EMG}$  vs wake). **e**, Mean correlation coefficient between delta power and NE level (5 min NREM sleep episodes). **f**, Three different example traces showing how optogenetic activation of locus coeruleus (LC, 2 s 20 Hz 10 ms pulses) during periods of NE descend leads to NE ascend followed by a delayed change in spindle occurrences and amplitude reduction of 7-15 bandpass filtered EEG that is not represented by sigma power (window = 5 s, overlap: 2.5 s).  $n=4$  (c);  $n=7$  (d, e). Data is shown as mean  $\pm$  SEM. \* $P < 0.05$ , \*\* $P < 0.01$ .



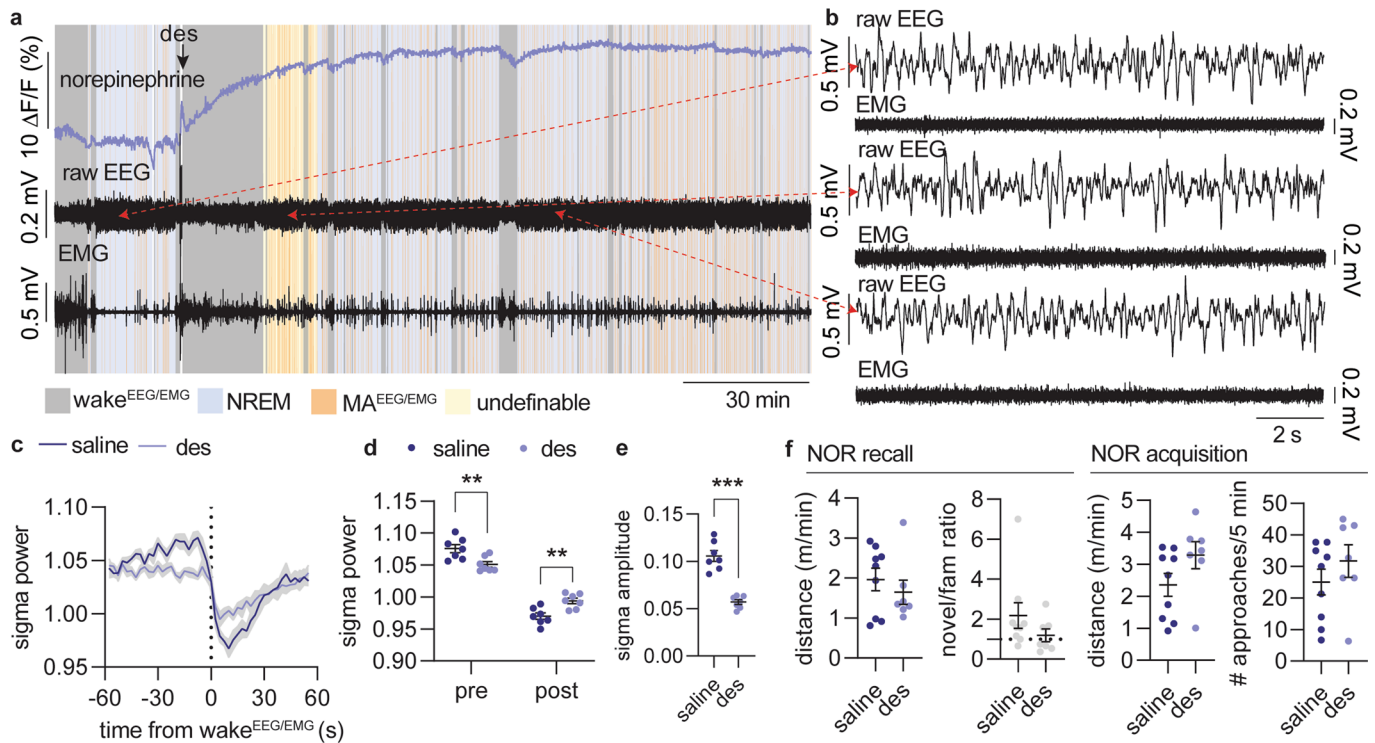
Extended Data Fig. 4 | See next page for caption.

**Extended Data Fig. 4 | Optogenetic suppression of LC.** **a**, Arch expression in LC was verified by co-staining for TH and GFP. Arrowheads indicate the tip location of the optic fiber (scale bar = 800  $\mu\text{m}$ ). **b**, Close up of **a** (scale bar = 400  $\mu\text{m}$ ). **c**, Example traces showing norepinephrine level, sigma power, sleep spindles, bandpass LFP in sigma range, and EMG raw data. **d**, Mean sigma power aligned to onset of NE drop (NREM and IS-REM) or onset of laser stimulation (Arch). **e**, Time spent in sleep/wake stages during 2-h recording between memory encoding and recall (2-way repeated measures ANOVA with Šídák's multiple comparison post hoc test). **f**, Number of laser stimulation (% of total number) in each sleep/wake stage (2-way repeated measures ANOVA with Šídák's multiple comparison post hoc test). **g**, Mean NE trace at laser onset during wakefulness. **h**, NE descent amplitude induced by laser onset during NREM and wakefulness (2-way repeated measures ANOVA with Šídák's multiple comparison post hoc test,  $P=0.0046$ , NRREM). **i**, Percentage of laser stimulations during wakefulness resulting in transition to NREM sleep (unpaired  $t$ -test). **j**, Distance moved and ratio between approaches during the recall phase of the novel object recognition (NOR) (two-tailed unpaired  $t$ -test,  $P=0.049$ , one-sample  $t$ -test  $P=0.49$ , YFP;  $P=0.026$ , Arch). **k**, Distance moved and object approaches during the acquisition phase of the NOR (unpaired  $t$ -test). **l**, Linear regression between object exploration ratio and time spent in REM sleep. **m**, Linear regression between object exploration ratio and number of REM bouts/h. **n**, Linear regression between object exploration ratio and mean theta power during REM sleep. **o**, Linear regression between object exploration ratio and time spent in NREM sleep. **p**, Linear regression between object exploration ratio and theta amplitude in response to laser. **q**, Linear regression between object exploration ratio and delta amplitude in response to laser.  $n=9$  Arch, 5 YFP. Data is shown as mean  $\pm$  SEM. \* $P < 0.05$ , \*\* $P < 0.01$ .





**Extended Data Fig. 5 | Optogenetic activation of LC.** **a**, Distance moved and ratio between novel and familiar object approaches during recall phase of novel object recognition (ratio: two-tailed unpaired *t*-test,  $P = 0.052$ ; one-sample *t*-test,  $P = 0.035$ , YFP;  $P = 0.64$ , Chr2). **b**, Distance moved and object exploration during memory acquisition (right).  $n = 7$  Chr2, 7 YFP. Data is shown as mean  $\pm$  SEM. \* $P < 0.05$ .



**Extended Data Fig. 6 | The effect of NE reuptake inhibition on EEG and arousability.** **a**, Representative traces of norepinephrine, raw EEG and EMG before and after administration of the NE reuptake inhibitor, desipramine (des, 10 mg/kg). **b**, Example EEG and EMG traces from NREM sleep prior to desipramine administration (top), during undefinable phases following desipramine administration (middle) and from defined NREM sleep following administration with desipramine (bottom). **c**, Sigma power traces aligned to the onset of awakenings (wake<sup>EEG/EMG</sup>) following either treatment with saline or desipramine. **d**, Mean sigma power before and after NREM-wake<sup>EEG/EMG</sup> transition (2-way repeated measures ANOVA with Šídák's multiple comparison post hoc test,  $P=0.0024$ , pre;  $P=0.031$ , post). **e**, Reduction in sigma power amplitude (two-tailed paired  $t$ -test,  $P=0.0007$ ). **f**, Distance moved and ratio between novel and familiar object approaches during the recall phase of the novel object recognition (NOR) as well as distance moved and number of object approaches during the acquisition phase (unpaired  $t$ -test and one-sample  $t$ -test).  $n=7$  (c-e),  $n=7$  des, 9 sal (f). Data is shown as mean  $\pm$  SEM.  $**P<0.01$ ,  $***P<0.001$ .

## Reporting Summary

Nature Portfolio wishes to improve the reproducibility of the work that we publish. This form provides structure for consistency and transparency in reporting. For further information on Nature Portfolio policies, see our [Editorial Policies](#) and the [Editorial Policy Checklist](#).

### Statistics

For all statistical analyses, confirm that the following items are present in the figure legend, table legend, main text, or Methods section.

n/a Confirmed

- |                                     |                                     |  |
|-------------------------------------|-------------------------------------|--|
| <input type="checkbox"/>            | <input checked="" type="checkbox"/> | The exact sample size ( $n$ ) for each experimental group/condition, given as a discrete number and unit of measurement  |
| <input type="checkbox"/>            | <input checked="" type="checkbox"/> | A statement on whether measurements were taken from distinct samples or whether the same sample was measured repeatedly  |
| <input type="checkbox"/>            | <input checked="" type="checkbox"/> | The statistical test(s) used AND whether they are one- or two-sided<br><i>Only common tests should be described solely by name; describe more complex techniques in the Methods section.</i>   |
| <input checked="" type="checkbox"/> | <input type="checkbox"/>            | A description of all covariates tested   |
| <input type="checkbox"/>            | <input checked="" type="checkbox"/> | A description of any assumptions or corrections, such as tests of normality and adjustment for multiple comparisons  |
| <input type="checkbox"/>            | <input checked="" type="checkbox"/> | A full description of the statistical parameters including central tendency (e.g. means) or other basic estimates (e.g. regression coefficient) AND variation (e.g. standard deviation) or associated estimates of uncertainty (e.g. confidence intervals) |
| <input type="checkbox"/>            | <input checked="" type="checkbox"/> | For null hypothesis testing, the test statistic (e.g. $F$ , $t$ , $r$ ) with confidence intervals, effect sizes, degrees of freedom and $P$ value noted<br><i>Give <math>P</math> values as exact values whenever suitable.</i>                            |
| <input checked="" type="checkbox"/> | <input type="checkbox"/>            | For Bayesian analysis, information on the choice of priors and Markov chain Monte Carlo settings   |
| <input checked="" type="checkbox"/> | <input type="checkbox"/>            | For hierarchical and complex designs, identification of the appropriate level for tests and full reporting of outcomes   |
| <input checked="" type="checkbox"/> | <input type="checkbox"/>            | Estimates of effect sizes (e.g. Cohen's $d$ , Pearson's $r$ ), indicating how they were calculated   |

*Our web collection on [statistics for biologists](#) contains articles on many of the points above.*

### Software and code

Policy information about [availability of computer code](#)

Data collection Synapse v. 96 (Tucker Davis Technologies), SleepScore (ViewPoint Behavior Technology), Ethovision XT 11.5 (Noldus), NIS-Elements (Nikon)

Data analysis Matlab R2020a, Prism 9.3, (GraphPad), ImageJ, SleepScore (ViewPoint Behavior Technology), Ethovision XT 11.5 (Noldus). The custom-made MatLab code used during the current study are available from GitHub: <https://github.com/MieAndersen/NE-oscillations>

For manuscripts utilizing custom algorithms or software that are central to the research but not yet described in published literature, software must be made available to editors and reviewers. We strongly encourage code deposition in a community repository (e.g. GitHub). See the Nature Portfolio [guidelines for submitting code & software](#) for further information.

### Data

Policy information about [availability of data](#)

All manuscripts must include a [data availability statement](#). This statement should provide the following information, where applicable:

- Accession codes, unique identifiers, or web links for publicly available datasets
- A description of any restrictions on data availability
- For clinical datasets or third party data, please ensure that the statement adheres to our [policy](#)

The datasets generated during and/or analysed during the current study are available from the corresponding author upon reasonable request.

## Field-specific reporting

Please select the one below that is the best fit for your research. If you are not sure, read the appropriate sections before making your selection.

- Life sciences       Behavioural & social sciences       Ecological, evolutionary & environmental sciences

For a reference copy of the document with all sections, see [nature.com/documents/nr-reporting-summary-flat.pdf](https://www.nature.com/documents/nr-reporting-summary-flat.pdf)

## Life sciences study design

All studies must disclose on these points even when the disclosure is negative.

Sample size	No statistical methods were used to pre-determine sample size in these exploratory studies, but our sample sizes are similar to those reported in previous publications and the animal-to-animal variability observed during the experiments
Data exclusions	Mice with poor expression of fluorescent indicators or noisy EEG/EMG signals were excluded from the study.
Replication	Main findings in Fig. 1 and 2 were reproduced across several differing experiments as the control groups in the manipulation experiments displayed the same patterns of signaling.
Randomization	Animals in test and control groups were litter mates and randomly selected. Conditions were counterbalanced across mice.
Blinding	Investigators were blinded to the conditions as wide as possible (behavioral tasks). Some experiments were not blinded, because the experimental conditions were obvious to the researchers or since all data acquisition and analysis were automated. All measurements were subsequently analyzed applying the same automated criteria.

## Reporting for specific materials, systems and methods

We require information from authors about some types of materials, experimental systems and methods used in many studies. Here, indicate whether each material, system or method listed is relevant to your study. If you are not sure if a list item applies to your research, read the appropriate section before selecting a response.

### Materials & experimental systems

n/a	Involved in the study
<input type="checkbox"/>	<input checked="" type="checkbox"/> Antibodies
<input checked="" type="checkbox"/>	<input type="checkbox"/> Eukaryotic cell lines
<input checked="" type="checkbox"/>	<input type="checkbox"/> Palaeontology and archaeology
<input type="checkbox"/>	<input checked="" type="checkbox"/> Animals and other organisms
<input checked="" type="checkbox"/>	<input type="checkbox"/> Human research participants
<input checked="" type="checkbox"/>	<input type="checkbox"/> Clinical data
<input checked="" type="checkbox"/>	<input type="checkbox"/> Dual use research of concern

### Methods

n/a	Involved in the study
<input checked="" type="checkbox"/>	<input type="checkbox"/> ChIP-seq
<input checked="" type="checkbox"/>	<input type="checkbox"/> Flow cytometry
<input checked="" type="checkbox"/>	<input type="checkbox"/> MRI-based neuroimaging

## Antibodies

### Antibodies used

Primary antibodies: anti-RFP antibody (1:500, Abcam, Cat#:ab62341), Anti-GFP, Chicken Antibodies, IgY Fraction (1:500, Aves, Cat#:GFP-1020), GFP Polyclonal Antibody (1:500, Thermo Fisher Scientific, Cat#:A-6455), Mouse Anti-Neuronal Nuclei (NeuN) Monoclonal Antibody, clone A60 (1:100, Merck Millipore, Cat#:MAB377), Anti-Tyrosine Hydroxylase, clone LNCl (1:500, Merck Millipore, Cat#:MAB318). Goat anti-Rabbit IgG (H+L) Highly Cross-Adsorbed Secondary Antibody, Alexa Fluor 488 (Thermo Fisher Scientific A11034), Goat anti-Chicken IgY (H+L) Secondary Antibody, Alexa Fluor 488 (Thermo Fisher Scientific A11039), Goat anti-Rabbit IgG (H+L) Cross-Adsorbed Secondary Antibody, Alexa Fluor 568 (Thermo Fisher Scientific A11011), Goat anti-Chicken IgY (H+L) Secondary Antibody, Alexa Fluor 568 (Thermo Fisher Scientific A11041), Goat anti-Mouse IgG1 Cross-Adsorbed Secondary Antibody, Alexa Fluor 647 (Thermo Fisher Scientific A21240).

### Validation

Primary antibodies against against GFP (49 references, <https://www.aveslabs.com/products/anti-green-fluorescent-protein-antibody-gfp>, 249 references, <https://www.thermofisher.com/order/genome-database/details/antibody/A-6455.html>), RFP (237 references, [https://www.abcam.com/RFP-antibody-ab62341.html?gclid=Cj0KCQjwg\\_itBhDrARIsAD31b5jts9XHPaivWVclmi6HUaamlbSxfbedlQ3KqMW5HI3pXOoVttppccRsaAgMiEALw\\_wcB](https://www.abcam.com/RFP-antibody-ab62341.html?gclid=Cj0KCQjwg_itBhDrARIsAD31b5jts9XHPaivWVclmi6HUaamlbSxfbedlQ3KqMW5HI3pXOoVttppccRsaAgMiEALw_wcB)), and NeuN (references on [https://www.merckmillipore.com/DK/en/product/Anti-NeuN-Antibody-clone-A60,MM\\_NF-MAB377#anchor\\_REF](https://www.merckmillipore.com/DK/en/product/Anti-NeuN-Antibody-clone-A60,MM_NF-MAB377#anchor_REF)) are widely used and well-validated. In addition the mouse anti-TH has been used in another study to immunostain locus coeruleus in brain slices from mice (Nomura et al., 2014).



## Animals and other organisms

Policy information about [studies involving animals](#); [ARRIVE guidelines](#) recommended for reporting animal research

### Laboratory animals

We used group-housed male and female C57BL/6J mice (ordered from Janvier) and TH:Cre (Jackson Stock No: 008601) mice bred in house (heterozygous versus wildtype breeding). Mice were maintained on a 12:12 light cycle (lights on at 07:00) at 21 degrees C with 40-60% humidity with water and food ad libitum. Mice were 12-20 weeks at time of experiments.

### Wild animals

The study did not involve wild animals

### Field-collected samples

The study did not involve samples collected from the fields

### Ethics oversight

All experiments were approved by the Danish Animal Experiments Inspectorate and were overseen by the University of Copenhagen Institutional Animal Care and Use Committee (IACUC), in compliance with the European Communities Council Directive of 22 September 2010 (2010/63/EU) legislation governing the protection of animals used for scientific purposes.

Note that full information on the approval of the study protocol must also be provided in the manuscript.